

1 **Chronology and sedimentology of a new 2.9 ka annually laminated record from South**  
2 **Sawtooth Lake, Ellesmere Island**

3

4 **Francois Lapointe<sup>1,2</sup>, Pierre Francus<sup>2,3</sup>, Joseph S. Stoner<sup>4</sup>, Mark B. Abbott<sup>5</sup>, Nicholas**  
5 **L. Balascio<sup>6</sup>, Timothy L. Cook<sup>1</sup>, Raymond S. Bradley<sup>1</sup>, Steven L. Forman<sup>8</sup>, Mark**  
6 **Besonen<sup>9</sup>, Guillaume St-Onge<sup>3,10</sup>.**

7

8 <sup>1</sup>Climate Science Center, Department of Geosciences, University of Massachusetts,  
9 Amherst, MA 01003, USA.

10

11 <sup>2</sup>Centre - Eau Terre Environnement, Institut National de la Recherche Scientifique,  
12 Canada Research Chair in Environmental Sedimentology, Québec, G1K 9A9, Canada.

13

14 <sup>3</sup>GEOTOP, Université du Québec à Montréal, Québec H3C 3P8, Montreal, H3C 3P8,  
15 Canada.

16

17 <sup>4</sup>College of Earth, Ocean, and Atmospheric Sciences, Oregon State University, Corvallis,  
18 OR 97331, USA.

19 <sup>5</sup>Department of Geology and Planetary Science, University of Pittsburgh, Pittsburgh, PA  
20 15260, USA.

21 <sup>6</sup>Department of Geology, College William and Mary, 251 Jamestown Road, Williamsburg  
22 VA 23187 USA.

23

24 <sup>1</sup>Worcester State University, 486 Chandler Street, Worcester, Massachusetts, 01602, USA.  
25

26 <sup>8</sup>Department of Geology, Baylor University, College of Arts and Sciences, One Bear  
27 Place #97354, Waco, Texas, TX 76798, USA.

28

29 <sup>9</sup>Harte Research Institute for Gulf of Mexico Studies, Texas A&M University - Corpus  
30 Christi, Corpus Christi, TX 78412, USA.

31

32 <sup>10</sup>Institut des sciences de la mer de Rimouski, Canada Research Chair in Marine Geology,  
33 Université du Québec à Rimouski, 310 allée des Ursulines, Rimouski, Québec, G5L 3A1,  
34 Canada.

35

36

37 **Keywords**

38 **Holocene; Arctic climate; Varves; Paleoclimatology; Chronology; Paleomagnetism**



40 **Abstract**

41 Few annually laminated (varved) lacustrine records exist in the Arctic, but these high-  
42 resolution climate archives are needed to better understand abrupt climate change and the  
43 natural mode of climate variability of this sensitive region. This paper presents a new high-  
44 resolution 2900-year long varved lake sediment record from the Fosheim Peninsula,  
45 Ellesmere Island. The varve chronology is based on multiple varve counts made on high-  
46 resolution scanning electron microscope images of overlapping sediment thin sections, and  
47 is supported by several independent dating techniques, including  $^{137}\text{Cs}$  and  $^{210}\text{Pb}$  analysis,  
48 one optically stimulated luminescence age located close to the bottom of the composite  
49 sequence, and comparison between paleomagnetic variations of this record and the longest  
50 High-Arctic varve record, Lower Murray Lake, which confirms the reliability of the  
51 Sawtooth chronology. High resolution backscattered images examined under a scanning  
52 electron microscope (SEM) were crucial to giving a more detailed view of sedimentation  
53 processes in the lake and thus help to delineate varves more precisely than in conventional  
54 image analysis. Fine-scale geochemical analysis reveals that lake sedimentation is mainly  
55 clastic and that elemental geochemistry is influenced by grain-size. Principal component  
56 analysis of multiple proxies and the coarse grain-size fraction of South Sawtooth Lake  
57 display similar fluctuations to the nearby Agassiz Ice Cap  $\delta^{18}\text{O}$  record, including lower  
58 values during the Little Ice Age cold period. These results show this new high-resolution  
59 and continuous record has a reliable varve chronology and is sensitive to temperature  
60 variability. South Sawtooth Lake's mean sedimentation rate of  $1.67 \text{ mm a}^{-1}$  is higher than  
61 any other sedimentary sequence in the High Arctic providing a unique opportunity for  
62 extracting new, high-resolution paleoclimatological and paleoenvironmental record.

63

64

65

66

67

68

69

70

71 **1. Introduction**

72

73 The Arctic has undergone substantial warming during the last decade. This trend is  
74 expected to increase with further loss of sea-ice and increased glacier melt, thus  
75 accelerating the related positive feedback processes. Due to limited instrumental data from  
76 the region, there is still a huge lack of understanding of the Arctic climate system (Cohen  
77 et al., 2014). High-resolution climate records can provide meaningful information about  
78 past temperature and precipitation (Lapointe et al., 2017). However, published climate  
79 archives from the region are insufficient and their spatial distribution is limited in extent.  
80 Development of reliable paleoclimate records from the High Arctic is especially  
81 challenging given the limited success of radiocarbon dating as a means of constraining the  
82 chronology of lacustrine records from Arctic lakes. This is largely caused by limited  
83 biological productivity and the presence of aged carbon stored in watersheds which often  
84 leads to unreliable age determinations (Abbott and Stafford, 1996). In contrast, the  
85 precision and accuracy of varve-count chronologies can provide superior chronologies  
86 compared to those based purely on radiometric methods (Zolitschka et al., 2015). Yet new  
87 annually laminated records from the Canadian Arctic must be tested against other  
88 independent dating methods to demonstrate that they are indeed varves. This paper  
89 provides a new varved record from South Sawtooth Lake, Ellesmere Island (hereafter,  
90 SSL). The varve chronology is supported by several independent dating techniques,  
91 including radiometric analysis of the recent record, optically stimulated luminescence  
92 dating (OSL), and paleomagnetic variations over the past 2900 years. This paper is an  
93 extension of previous work undertaken at SSL (Francus et al., 2002) using new sediment  
94 cores to establish a chronology and characterize the stratigraphy. We then extract physical  
95 and geochemical properties of the sediment in order to establish a basis for further  
96 paleoclimatic investigations using this record.

97

98 **1.1 Study site**

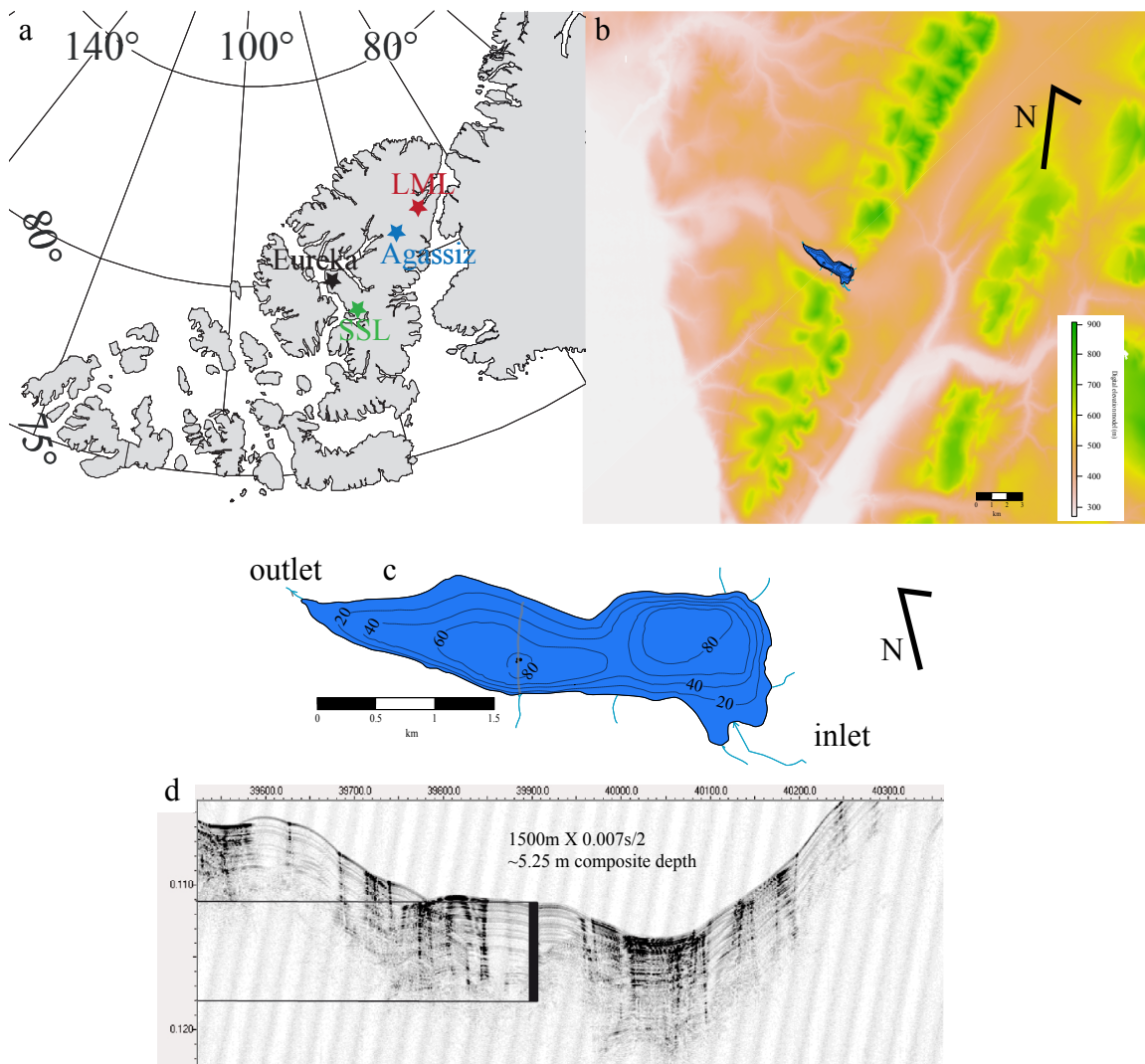
99

100 SSL (79° 20'N, 83°51'W, 280 m a.s.l.) is located on the Fosheim peninsula in the Eastern  
101 Canadian High-Arctic (Fig. 1). This site has been the focus of several studies (Francus et

102 al., 2002; Perren et al., 2003; Lewis et al., 2005; Francus et al., 2008), which indicate that  
103 sediments in the lake are varved. The surficial geology of the area is composed of blanket  
104 and veneer tills. Deglaciation started around 5800 BCE (7800 B.P.) with present-day  
105 conditions reached around 4300 BCE (6300 B.P.) (England, 1983). The bedrock geology  
106 of the SSL watershed is composed mainly of Triassic sandstones and calcareous siltstones,  
107 with minor concentrations of limestone and shale (Geological Survey of Canada 1972).  
108 The lake and its watershed surface area are  $\sim 2.6 \text{ km}^2$  and  $47 \text{ km}^2$ , respectively, with a  
109 maximum elevation of  $\sim 915 \text{ m a.s.l.}$  A single tributary spills into the lake from the  
110 southeast, while the outlet is situated at the northwestern end (Francus et al., 2008). SSL is  
111 an elongated lake divided into a proximal and a distal basin (100 and 82 m deep,  
112 respectively) separated by a 60-m deep sill. This configuration limits erosion in the distal  
113 basin, where the sediment cores were recovered (e.g. Francus et al., 2008). A seismic  
114 survey was conducted in 2006 revealing that the distal basin is devoid of major mass  
115 movement deposits (Fig. 1b,c), and thus well suited for paleoclimatological investigations.

116 The geomorphic setting of the study area with its surrounding mountains and highlands  
117 limit the incursion of cold Arctic Ocean air masses and cyclonic activity from Baffin Bay  
118 (Edlund and Alt, 1989). From 1948-2016, the average monthly temperature at Eureka (the  
119 nearest weather station, 84 km to the NW and 10m asl), were 2.5, 5.9, and 3.3 °C during  
120 June, July and August, respectively. Described as an extreme polar desert, the region's  
121 annual precipitation is 65 mm and  $\sim 25 \text{ mm}$  falls as rain according to the Eureka weather  
122 station. However, a temporary weather station at SSL recorded twice the amount of rain  
123 recorded at Eureka (Lewis et al., 2002). Precipitation for June and July of 1994 at a nearby  
124 site in the Sawtooth Range reached 64 mm, similar to the mean annual value at Eureka  
125 (Lewkowicz and Hartshorn, 1998). It is also worth mentioning that great amounts of rain  
126 were witnessed during the field season of 2012 at SSL in the end of May, although no rain  
127 was recorded at Eureka during that time. Thus, the orographic influence on climate  
128 combined with the steep slopes with elevation reaching  $\sim 915 \text{ m asl}$  (Fig. 1b) promote  
129 hillslope processes and sediment transfer into the lake, resulting in SSL having one of the  
130 highest sedimentation rates in the region (Francus et al., 2008).

131 The annual couplets result from seasonal differences in the lake. Clay caps are formed by  
 132 the settling of fine clay particles during the winter when the lake is ice-covered (2-3 m  
 133 thick ice) and the turbulence in the water column is low to absent. In turn, deposition of  
 134 coarser sediments associated with overflows triggered by early snow melt and occasional  
 135 rainfall events occurs later in the summer season (Francus et al., 2008).  
 136  
 137



138  
 139 Figure 1. a) Location of South Sawtooth Lake in the Canadian Arctic, Ellesmere Island.  
 140 Green, red, blue and black stars denote South Sawtooth Lake (SSL) Lower Murray Lake  
 141 (LML), Agassiz Ice Cap and Eureka weather station, respectively. b) Land digital elevation  
 142 model (DEM) base map from the ArcticDEM 7 Polar Geoscience Center showing SSL in  
 143 the Sawtooth Range. Map created in R. c) SSL bathymetry showing SS12-12, the location

144 of the composite sequence (black circles). The grey line crossing the lake corresponds to  
145 the seismic profile in d. d) SEG-Y data from the seismic profile were processed using the  
146 *Kingdom Suite*<sup>®</sup>. Subbottom data were collected in the lake using a Edge Tech 3100 Chirp  
147 at a frequency 4-24 kHz.

148  
149

150

## 151 **2 Methods**

### 152 **2.1 Chronology**

#### 153 **2.1.1 Cores, thin sections and imageries**

154

155 Overlapping core sections were recovered from three holes drilled in the lake-ice surface  
156 at the deepest water depth location (82 m) in June 2012. A total of 15 core sections were  
157 retrieved using a UWITEC percussion corer equipped with a locking piston allowing for  
158 multiple drives to be recovered from each hole. Cores were first analysed using a Siemens  
159 SOMATOM Definition AS+ 128 CT-Scanner at INRS in Québec City in order to establish  
160 the composite sequence. The upper 4.98 m contains finely laminated sediments, which is  
161 the focus of this analysis. A total of 35 metal trays (each 19 cm long), filled with sediment  
162 removed from the cores (Francus and Asikainen, 2001), were first flash frozen by slow  
163 immersion in liquid nitrogen and then subsequently freeze dried (Normandeau et al., 2019).  
164 These 19 cm-long sediment profiles were collected in order to have a 1 cm overlap between  
165 them.

166 Dried sediment in the trays was then impregnated with epoxy resin (Lamoureux, 1994) and  
167 100 overlapping thin sections were made to cover the laminated interval. Thin sections  
168 (sediment exposed ~5 x 2 cm) were digitized using a flatbed scanner at 2400 dpi (1 pixel  
169 = 10.6 µm). Using the image analysis software package developed at INRS (Francus and  
170 Nobert, 2007), regions of interest (ROIs) were identified on the digital images. ROIs were  
171 labeled with three character alphabetic codes such as “aag” (see Figure 2b,c for an  
172 example). A Zeiss Evo<sup>®</sup> 50 scanning electron microscope (SEM) was then used to acquire  
173 ~8000 images in backscattered mode following the methods of Lapointe et al., (2012).  
174 These high-resolution images were used to count varves as they provide superior contrast  
175 relative to optical images and because many laminae are less than 0.5 mm and hard to  
176 delineate using digital flatbed scan images, or other common techniques.

177

### 178 **2.1.2 Radiometric dating**

179 The uppermost part (18.25 cm) of a gravity core (undisturbed sediment) were extruded in  
180 the field and measured continuously at a 1 cm increment for radionuclides ( $^{210}\text{Pb}$ ,  $^{137}\text{Cs}$ ) at  
181 the University of Pittsburgh.  $^{210}\text{Pb}$  and  $^{137}\text{Cs}$  activities were measured using a Canberra  
182 Gamma Spectrometer. The chronology was established using the constant rate of supply  
183 (CRS) model (Appleby, 2002).

184

### 185 **2.1.3 Paleomagnetic variations**

186 Paleomagnetic secular variations were derived from U-channel samples that were analyzed  
187 through progressive alternating field (AF) demagnetization measured at 1 cm intervals,  
188 using a 2G Enterprises<sup>TM</sup> model 755-1.65UC superconducting rock magnetometer at the  
189 Oregon State University's Paleo- and Environmental Magnetism Laboratory. The natural  
190 remanent magnetization (NRM) was measured and progressively demagnetized using  
191 stepwise AF up to 70 mT in 5 mT steps to isolate the characteristic remanent magnetization  
192 (ChRM) and collect the inclination of the ChRM. U-channel results were processed using  
193 the UPmag software (Xuan and Channell, 2009).

194

195

### 196 **2.1.4 Optically Simulated Luminescence dating**

197

198 Optically stimulated luminescence (OSL) dating provides a measure of time since sediment  
199 grains were deposited and shielded from further light exposure, which often effectively  
200 resets the luminescence signal to a low defineable level (Murray and Olley, 2002). A time-  
201 dependent luminescence signal is acquired upon buried with exposure to ionizing radiation  
202 ( $\alpha$ ,  $\beta$  and  $\gamma$ ) from the decay of radioisotopes in the surrounding sediments. This exposure  
203 to ionizing radiation and to a lesser extent, to cosmic radiation, results in displaced  
204 electrons within the quartz crystal lattice, with a proportion of this acquired charge  
205 increasing with time, named as a luminescence emission.

206

207 Single aliquot regeneration (SAR) protocols (Murray and Wintle, 2003; Wintle and  
208 Murray, 2006) were used in this study to estimate the apparent equivalent dose of the 44-  
209 20  $\mu\text{m}$  quartz fraction for 58 to 86 separate aliquots (Table 1). Each aliquot contained  
210 approximately 100 to 500 quartz grains corresponding to a 1 millimeter circular diameter  
211 of grains adhered (with silicon) to a 1 cm diameter circular aluminum disc. This aliquot  
212 size was chosen to maximize light output for the natural emissions with excitation; smaller  
213 aliquots often yielded insufficient emissions ( $<400$  photon counts  $\text{s}^{-1}$ ).

214 The quartz fraction was isolated by density separations using the heavy liquid Na-  
215 polytungstate, and a 40-minute immersion in HF (40%) was applied to **etch** the outer  $\sim 10$   
216  $\mu\text{m}$  of grains, which is affected by alpha radiation (Mejdahl and Christiansen, 1994).  
217 Finally, quartz grains were rinsed in HCl (10%) to remove any insoluble fluorides. The  
218 purity of quartz separates was evaluated by petrographic inspection and point counting of  
219 a representative aliquot. The purity of quartz separates was tested by exposing aliquots to  
220 infrared excitation (1.08 watts from a laser diode at  $845 \pm 4$  nm), which preferentially  
221 excites feldspar minerals. Samples measured showed weak emissions ( $<200$   
222 counts/second), at or close to background counts with infrared excitation, and ratio of  
223 emissions from blue to infrared excitation of  $>20$ , indicating a spectrally pure quartz extract  
224 (Duller et al., 2003).

225 An automated Risø TL/OSL-DA-15 system (Bøtter-Jensen et al., 2000) was used for SAR  
226 analyses. Blue light excitation ( $470 \pm 20$  nm) was from an array of 30 light-emitting diodes  
227 that deliver  $\sim 15$   $\text{mW cm}^{-2}$  to the sample position at 90% power. Optical stimulation for all  
228 samples was completed at an elevated temperature ( $125$   $^{\circ}\text{C}$ ) using a heating rate of  $5^{\circ}\text{C s}^{-1}$ .  
229 <sup>1</sup>.

230

231 The U and Th content of the sediments, assuming secular equilibrium in the decay series  
232 and  $^{40}\text{K}$ , were determined by inductively coupled plasma-mass spectrometry (ICP-MS)  
233 analyzed by ALS Laboratories, Reno, NV. The beta and gamma doses were adjusted  
234 according to grain diameter to compensate for mass attenuation (Fain et al., 1999). A  
235 significant cosmic ray component between  $0.03$  and  $0.05$   $\text{mGy a}^{-1}$  was included in the  
236 estimated dose rate taking into account the current depth of burial (Prescott and Hutton,  
237 1994). A moisture content (by weight) of  $35 \pm 5$  % was used in dose rate calculations,

238 which reflects the variability in current field moisture conditions. More information about  
239 OSL can be found in the Supplementary data.

240

241

## 242 **2.2 Annual grain-size data**

243 The 8-bit gray-scale SEM images (1024 x 768 pixels) collected from thin sections were  
244 transformed into black and white to obtain particle measurements for each year of  
245 sedimentation (Francus and Pirard, 2004). For this study, several grain-size indices were  
246 measured including the median, 90<sup>th</sup>, and 99<sup>th</sup> percentile diameters (D50, D90 and D99,  
247 respectively), the standard deviation (SD), the maximum diameter (MaxD<sub>0</sub>) and the weight  
248 % of the following fractions : <16 μm, <20 μm, <30 μm, 16-33 μm, 33-69 μm and >69  
249 μm. Weight was calculated using the formula :  $((4/3)*\pi*((D_0/2)^3))*2.65$  with D<sub>0</sub> being the  
250 apparent disk diameter (Francus et al., 2002).

251

## 252 **2.3 μ-XRF analysis**

253 An ITRAX core scanner, available at INRS-ETE in Québec City, was used to measure  
254 high-resolution geochemical variations (Croudace et al., 2006) using a molybdenum tube.  
255 The data acquisition was performed with a 100 μm resolution and an exposure time of 15s.  
256 Voltage and current were 30 kV and 30 mA, respectively with count per second (cps)  
257 values ranging from 26,000-34,000. A dispersive energy spectrum is acquired for each  
258 measurement point and peak are integrals calculated for each element. All elements were  
259 normalized by the total number of counts for each spectrum expressed in thousands.

260

## 261 **2.4 Density proxies**

262 Tomodensitometric 3D images correspond to the 3D X-ray attenuation of the objects in the  
263 sample, where higher attenuations represent higher densities and higher atomic numbers  
264 (Duliu 1999). Cores were scanned with X-ray peak energy of 140 kV with 250 mA current.  
265 Tomograms measuring 512 X 512 pixels were acquired continuously at every 0.4 mm,  
266 along a 0.6 mm-thick slice resulting in an overlap of 0.2 mm between each tomogram. The  
267 open source ImageJ package was used to reconstruct longitudinal profiles from tomograms

268 using the DICOM format. Gray-level values from these DICOM folders correspond to the  
269 attenuation values expressed in Hounsfield Units (HU), a proxy for relative density  
270 (Duchesne et al., 2009, Fortin et al., 2013).

271

## 272 **2.5 Statistical Analysis**

273 Principal components analysis (PCA) was performed on the multiproxy dataset using  
274 « FactoMineR (v1.33) » package (Husson et al., 2016) of the software R (Team  
275 Development, 2008). Prior to the PCA, all proxy data were normalized.

276

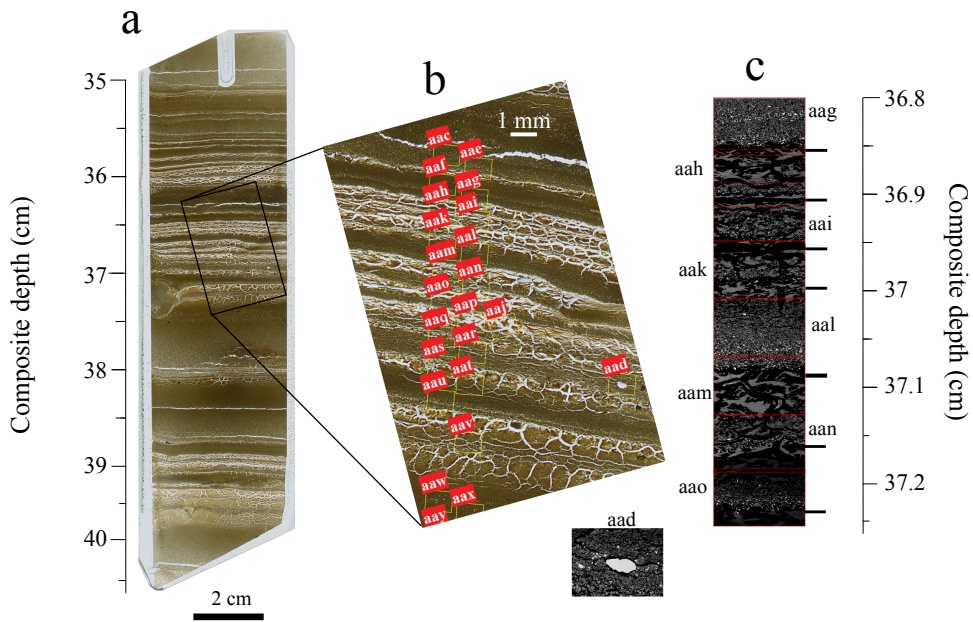
## 277 **3 Results and interpretations**

### 278 **3.1 Sedimentary facies and varve counting criteria**

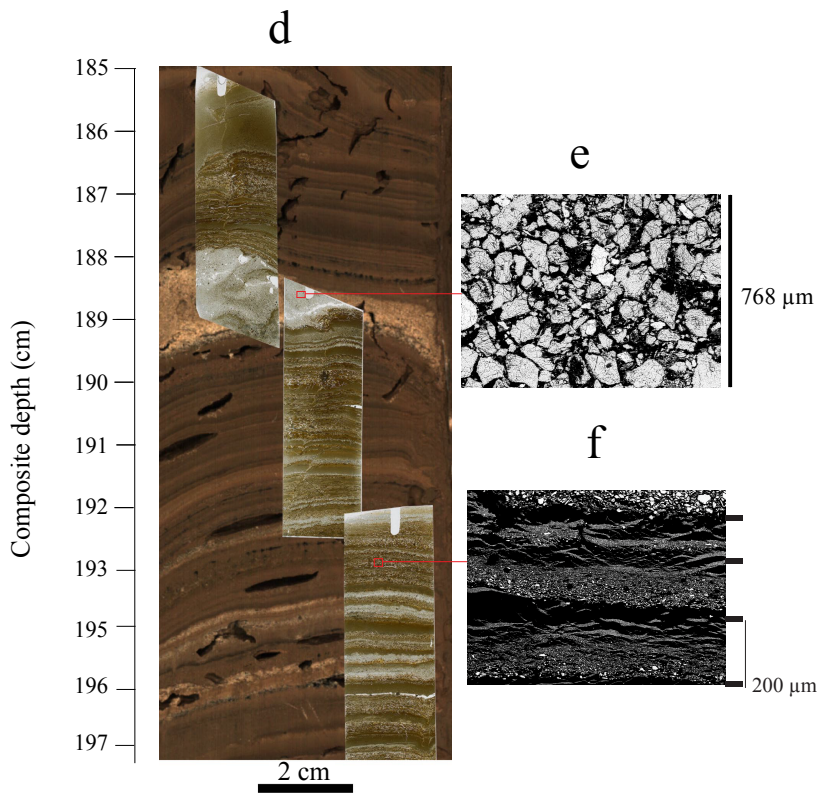
279 Varves found at SSL are mainly clastic, and six main facies were previously described  
280 (Francus et al., 2008). The most common lithofacies is composed of a fine silt layer  
281 deposited by nival melt runoff that is overlain by a clay cap. The clay caps, which are  
282 composed of clay-sized particles, and deposited during the 8 to 10 months of winter ice  
283 cover. These can be observed in backscattered SEM imageries as uniform light gray areas  
284 (Fig. 2c,f). As described in Francus et al., (2008), clay caps are typically distinguishable  
285 by wavy horizontal cracks formed when the sediments are freeze-dried during preparation  
286 of thin-sections. The clays caps represent the main feature used to delineate varves at SSL.  
287 Some density flow (sand laminae) deposits have also been observed (Fig. 2e), but there are  
288 only 38 of these units over a 2900-long varved sequence. Although the density flow facies  
289 can be triggered by rapidly deposited mass movement events, it can not be ruled out that  
290 they are the consequence of large rainfall events, thus climatologically-induced (Francus  
291 et al., 2008, Lapointe et al., 2012). Therefore, those layers are included in the chronology.  
292 Density flows are composed of a mixture of sediment and water in which the volume and  
293 mass of sediment exceeds that of water (Major, 2003). Thicker graded beds (Fig. 3e;  
294 turbidites) were also observed in the sequence and these are also different than the regular  
295 pattern of sedimentation. The base of a turbidite is typically poorly sorted and coarse  
296 grained as it is the result of an energetic turbiditic flow, in which finer particles are  
297 deposited after the coarse layer base as the flow wanes and further deposition occurs

298 through sediment settling (Mulder and Alexander, 2001). These beds have a median size  
299 of 2.3 mm (maximum: 51 mm). In rare instances (only 26 occurrences in the 2900 year  
300 sequence), dropstones or isolated grains can be found (Fig. 2; ROI: aad), and they are  
301 typically located within the upper part of the graded beds or within the clay caps themselves  
302 (e.g. Fig. 2; ROI aad). These isolated grains were not integrated in the grain-size analysis.  
303

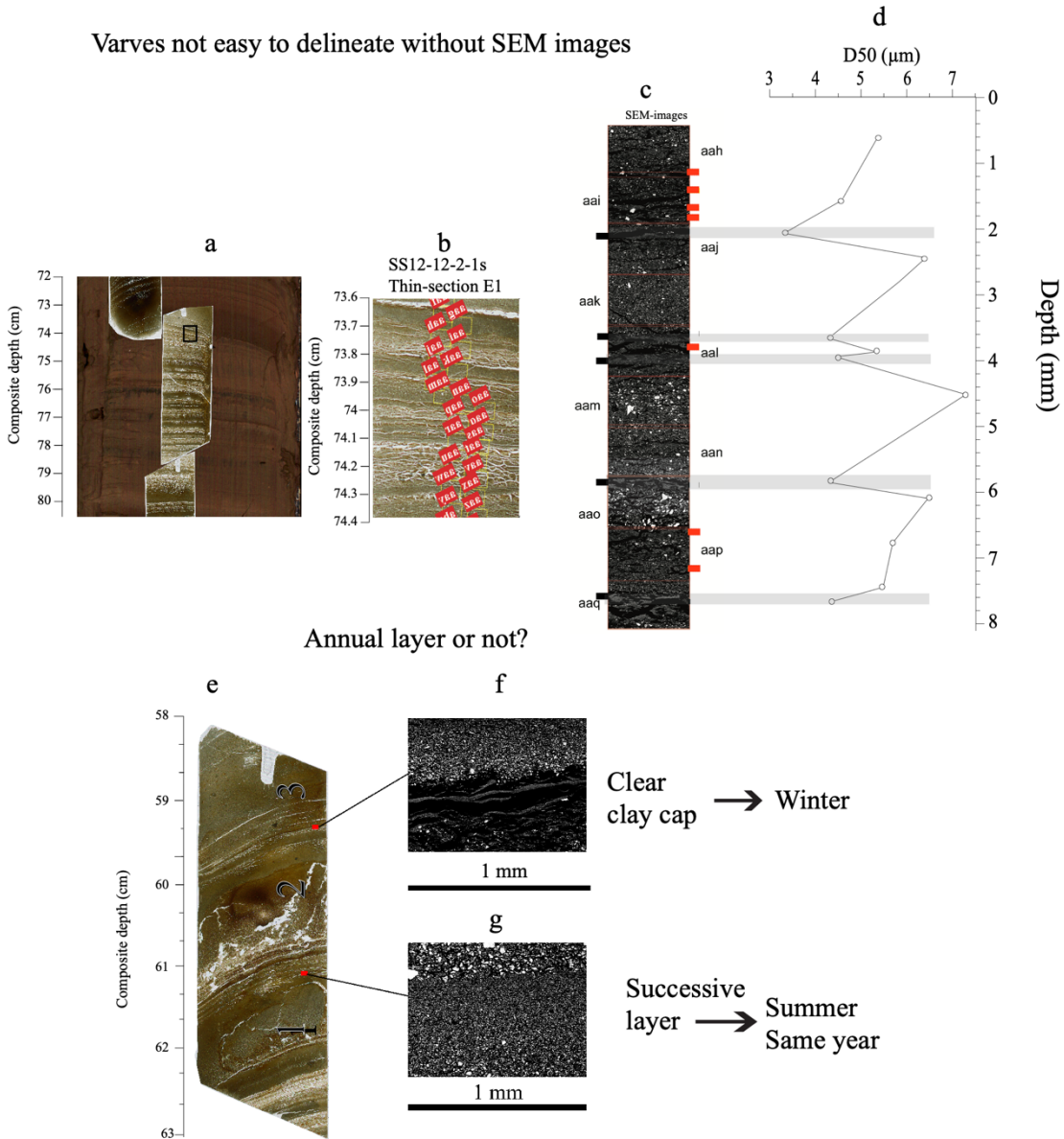
## Classical varves



## Density flow and thin classical varves



305 Figure 2. a) Flat-bed scan of thin section SS12-12-2-1s-C1. b) Enlargement of the black  
 306 rectangle with Regions of interest (ROIs) aac to aay. C) ROIs aag to aao acquired at the  
 307 scanning electron microscope are identified on the thin section, red rectangles are selected  
 308 ROIs (aag to aao). Black lines indicate varve boundaries. d) Section of ss12-12-2-2P  
 309 showing coarse grain size (e) and thin varves (f). High-resolution SEM imageries enhance  
 310 the ability to define varve boundaries. Black rectangles at the right of the SEM image  
 311 represent the varve boundaries. Note that the sand lamina presented in panel e is a density  
 312 flow, and has the coarsest grain-size of the entire varve record.  
 313



314 Figure 3. a) Same as Figure 2, but with thin section ss12-12-2-1s-E1. b) Zoom of the thin  
 315 section shown in a. c) SEM images of the corresponding ROIs. d) Median grain-size  
 316 variability according to the ROIs. Red horizontal bars in c) represent varve boundaries  
 317 made without SEM images. Black rectangles at the left of SEM-images in c represent clay  
 318

319 caps. e) Thin section SS12-12-2-1s D2 covering ~1600 CE – 1608 CE at 58.2 cm to 62.5  
320 cm composite depth. Three thick successive layers are observed. Red squares represent the  
321 two SEM images. f and g show a SEM-image of a clear clay cap (f) and a successive layer  
322 (g).  
323

324 Less than 2% of the varve intervals were not as easy to delineate (e.g. Fig. 3b). Analysis of  
325 these diffuse intervals relied on the superior contrast of SEM images compared to the thin  
326 section photographs (Fig. 3c). For example, red horizontal rectangles depict varve  
327 boundaries using the thin section photographs alone, while the black horizontal lines  
328 delimit varves based on inspection of the higher definition SEM images (Fig. 3c). As  
329 mentioned above, clay caps are typically distinguishable by wavy cracks when looking at  
330 thin section optical images. However, in conjunction with the presence of cracks (i.e. Fig.  
331 2f), there are a few wavy varves (< 25 over the past 2900 years) where silt sized detrital  
332 input can be detected as well (Figs. 3d, S1). These are unlikely to have been deposited  
333 during winter, when lakes are typically covered by at least 2 m of ice. Consequently, these  
334 layers are considered as making part of one single varve year. Hence, the backscatter  
335 electron (BSE) images give a more detailed view of sedimentation processes in the lake  
336 and thus help to delineate varves more precisely. These features were observed in intervals  
337 at 25.6 - 26.6 cm, 51.9 – 52.3 cm, 73.6 – 75.2 cm, 251.3 - 251.9 cm and 253.1 - 255.8 cm  
338 of the composite depth. These intervals are illustrated in Figure S2.

339

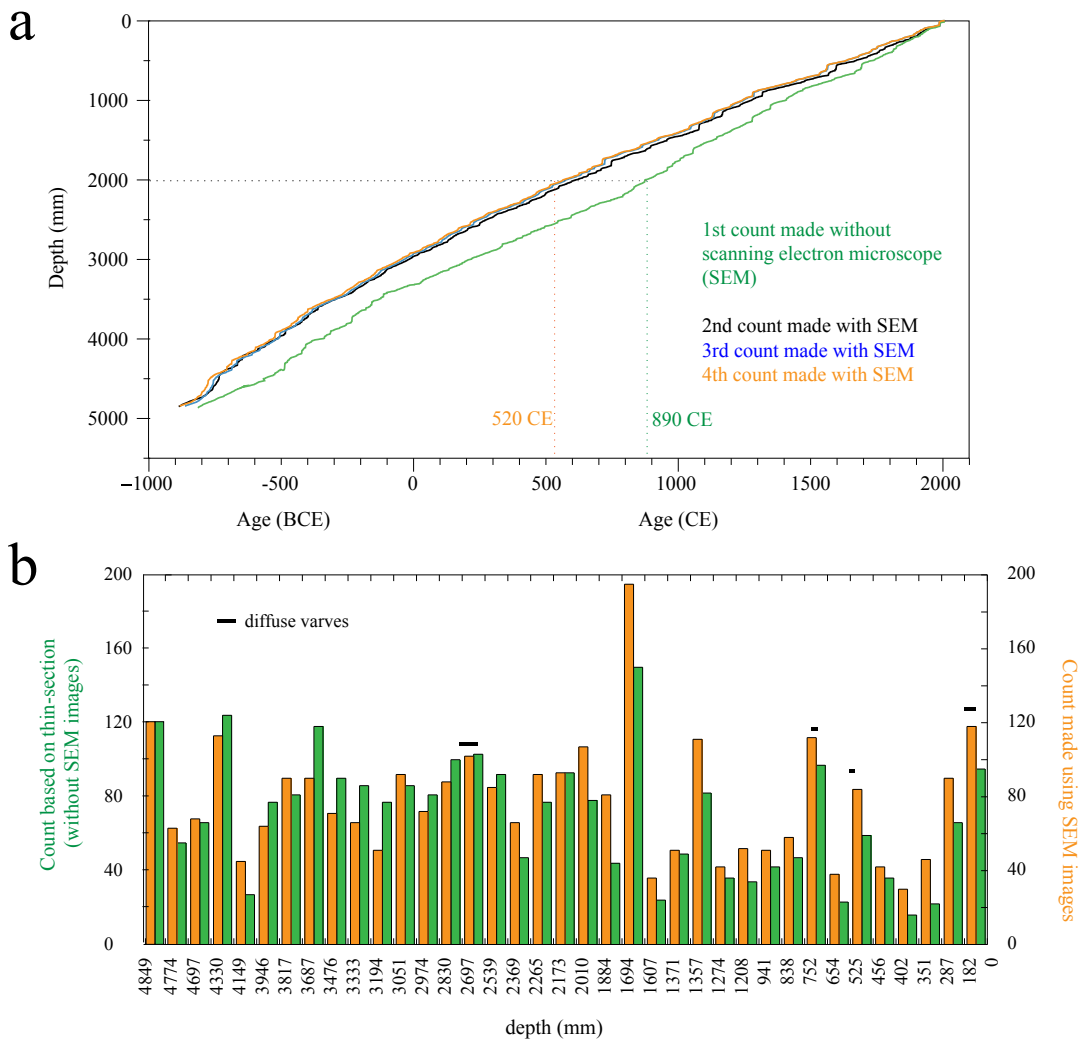
340 Intervals where successive, thick graded layers (> 10 mm) occur have more variable varve  
341 counts. These facies are characterized by coarser grain-size at their base and an upward  
342 fining sequence. It can be difficult to clearly identify whether these layers are the top of a  
343 turbidite sequence, a winter clay cap from a thick varve, or a sub-annual layer formed from  
344 a heavy summer rain event. As pointed out by Zolitschka et al., (2015), these features,  
345 which are related to a change in sedimentation rate, are hard to distinguish because they  
346 may be the result of several different hydrological events within the same season (e.g.  
347 rainfall, snowmelt, mass movement events). As an example, Figure 3e shows a thin section  
348 highlighting three successive thicker layers (> 1 cm). As shown in the BSE SEM images  
349 (Fig. 3g), there is a decrease in grain-size variation toward the top of the layer while the  
350 layer above it contains coarser material. Based only on the digital image of the thin section,

351 these can be interpreted as being individual annual layers, which is most likely the case for  
352 the upper SEM image (Fig. 3f). However, in the case of the lower SEM image (Fig. 3g)  
353 there is no obvious presence of a clay cap, and indeed this is more likely to be a successive  
354 layer event from the same year (Fig. 3g). Such successive layers occur only six times in  
355 the whole varved record (at 58.2 cm - 63.8 cm, 105.8 – 107.7 cm, 107 – 108 cm, 110.3 –  
356 112.2 cm, 129.2 – 131.7 cm, and 269 – 272.3 cm of the composite depth; see Fig. S3).  
357 Overall, the laminated sediments are unambiguous and well defined in the upper 4.9 m.

358

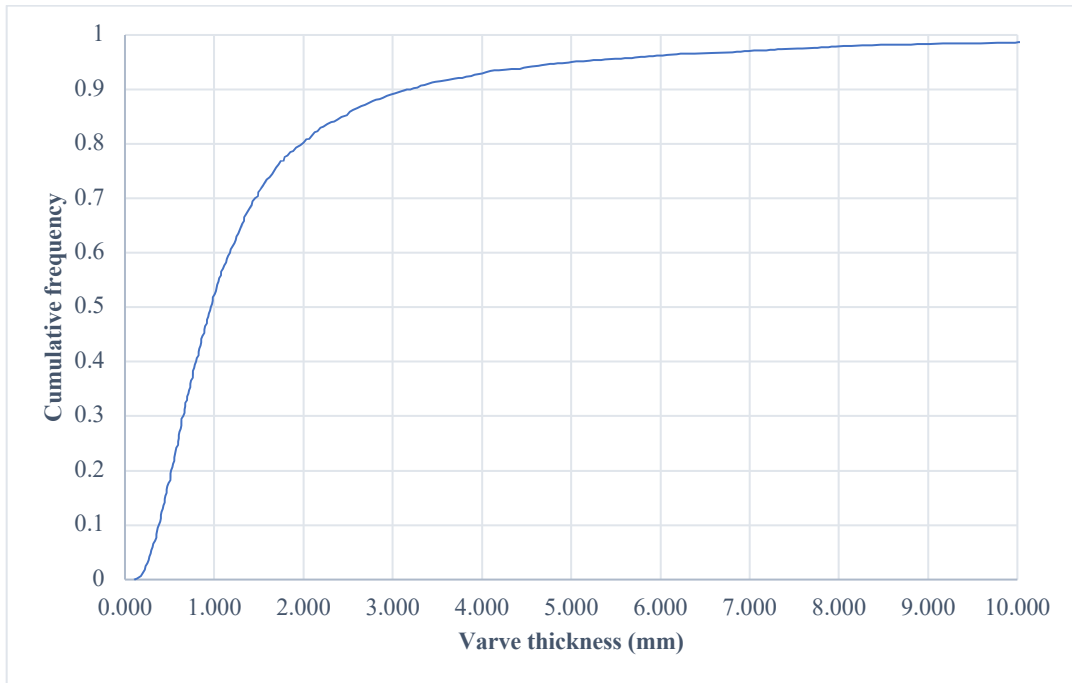
### 359 **3.2 Composite sequence of the SSL varve record**

360 The composite sequence is based on 100 thin sections extracted from nine overlapping core  
361 sections to obtain the most reliable continuous record (Fig. S1). One count was performed  
362 using thin-sections scans/photographs only, and three counts were made using SEM  
363 images. A total of 2900 varve years were identified (Figs. 4, 5, 6) in which 37  
364 stratigraphical markers (beds thicker than 0.8 cm) were used to compare varve counts  
365 between these layers (Fig. 4b). The three counts made using SEM images yield similar  
366 results with an overall difference of only 36 varves between the counts, or an estimated  
367 error of 1.2%, indicating that the varves can be delineated quite accurately (Fig. 6). Some  
368 discrepancies occur in those rare sections of the varve record that show a more diffuse  
369 pattern and when successive layers occur (e.g. Fig. 3). When comparing the varve counts  
370 based on optical images of thin sections (using a transparency flatbed scanner at 2400 dpi  
371 resolution), to one made using SEM images, the latter resulted in more varves being  
372 counted (Fig. 4). While the average varve thickness is 1.67 mm (Table S1), the median  
373 varve thicknesses is 0.96 mm (Table S2, Fig. 5), meaning that half of the varves are < 1  
374 mm in thickness, which are very challenging to delineate without high resolution SEM  
375 imagery. Cumulative frequency of the varve thicknesses distribution indicates that 90% of  
376 the varves are < 3 mm thick (Fig. 5). When the density flow deposits (turbidites and debris  
377 flow) are excluded from this analysis, the average varve thickness of this time series  
378 becomes 1.28 mm, but the median value does not change significantly (0.93 mm).



379

380 Figure 4. a) Four different varve counts: 1st made without the use of scanning electron  
 381 microscope (SEM) images (green); 2<sup>nd</sup> to 4<sup>th</sup> are counts made using SEM images. b)  
 382 Differences in varve counts between the 4<sup>th</sup> count made with SEM (orange) and the count  
 383 made without SEM (green) versus depth. Black horizontal rectangles identify diffuse  
 384 varves seen in the varve chronology.  
 385



386

387 Figure 5. Cumulative frequency of the varve thickness series. Note that half of the varve  
 388 thicknesses are less than 1 mm.

389

390

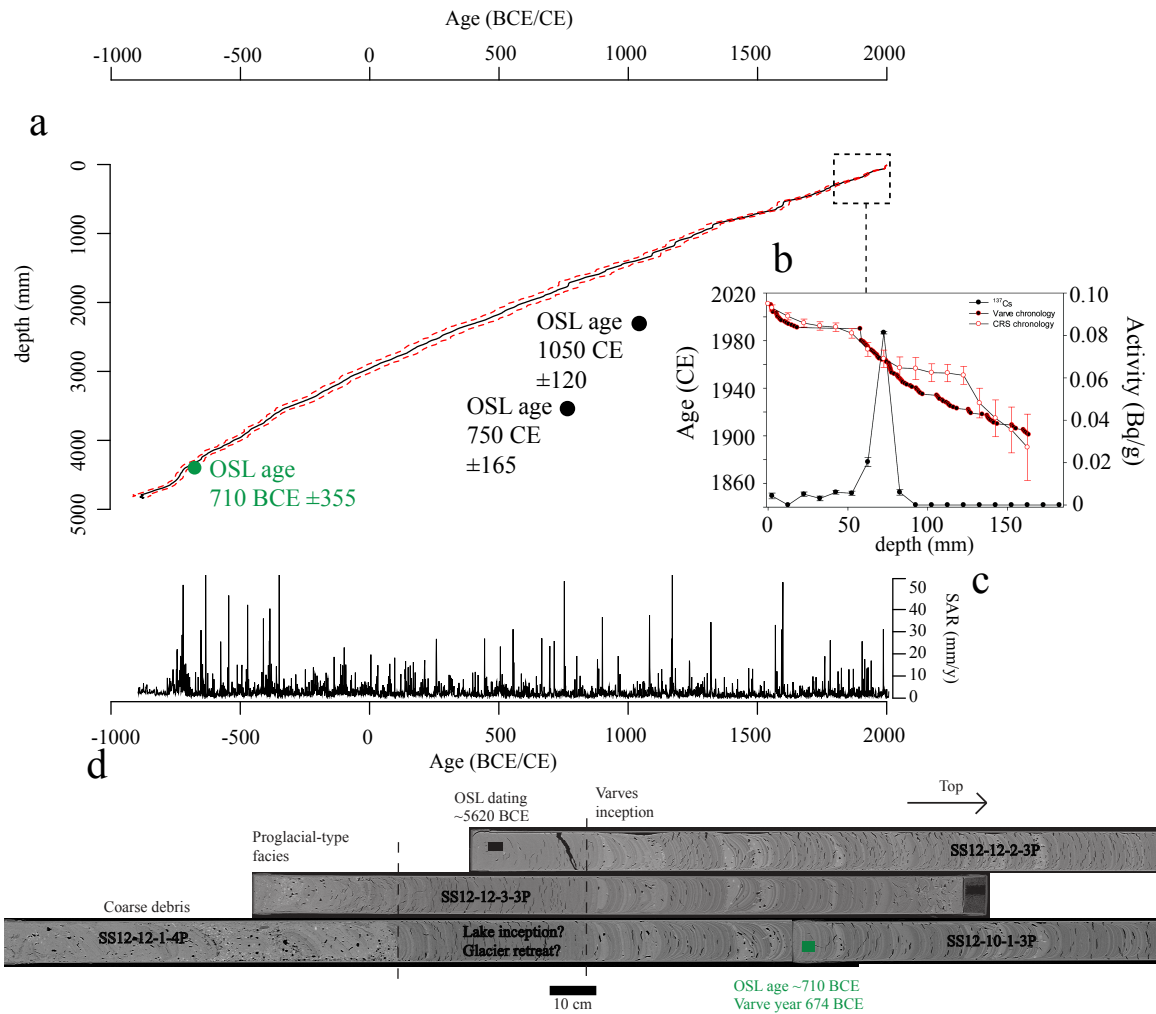
391

### 392 3.3 Independent Chronological Control

#### 393 3.3.1 Radiometric dating

394 For the upper 18.25 cm, the varve count compares well with the  $^{210}\text{Pb}$  CRS chronology  
 395 over the past 120 years (Fig. 6b). Furthermore, the  $^{137}\text{Cs}$  peak in 1963 matches the varve  
 396 counts when they are shifted by 9 years, which is in agreement with Francus et al., (2002)  
 397 who concluded that 9 years were eroded by a large basin-wide turbidite dated to 1990. This  
 398 means that 21 varves were deposited between 1990 and May of 2012 when the cores were  
 399 collected, providing additional evidence that this record is annually laminated.

400



401  
402  
403  
404  
405  
406  
407  
408  
409

Figure 6. a) Age model based on the three counts using SEM images. The red lines delimit the one standard deviation and the black line is the count average. Overall sedimentation rate is 1.67 mm a<sup>-1</sup>. b) <sup>137</sup>Cs activity, <sup>210</sup>Pb dating and varve count against depth. c) Sediment accumulation rates (mm a<sup>-1</sup>) based on the mean age-depth shown in a). d) Ct-Scan of sediment cores SS12-12-2-3P, SS12-12-3-3P, SS12-10-1-3P and SS12-12-1-4P with the location of 2 samples extracted for OSL dating (black and green rectangles).

410

### 411 3.3.2 Optically Stimulated Luminescence (OSL) dating

412

413 OSL dating of quartz grains for four samples from the cores further constrain the varve  
414 chronology (Table 1). The grains that yielded the OSL age of 7630  $\pm$  595 BP (5620 BCE)  
415 were sampled beneath the laminated section and above high-energy layers (core SS12-12-  
416 2-3P) that are likely related to pulses of a melting glacier, in what appears to be a

417 transitional period between the retreat of glacier in the watershed and the subsequent  
 418 inception of the lake (Fig. 6d – black rectangle). This age ( $\sim 5620 \pm 595$  BCE) is considered  
 419 to be reliable since the region is believed to have been fully deglaciated around  $\sim 5800$  BCE  
 420 (England, 1983). Moreover, it has low overdispersion (22%) and this age remained  
 421 unchanged at one sigma error with the addition of aliquots, and has a unimodal population  
 422 of equivalent dose. Thus, the age  $\sim 5620 \pm 595$  BCE can be viewed as secure. The OSL age  
 423 centered at 2720 (710 BCE), located close to onset of lacustrine infill, agrees at one sigma  
 424 error with the varve chronology ( $674 \text{ BCE} \pm 28$ ) (Fig. 6a, and Fig 6d – green rectangle).  
 425 Two other OSL ages centered at 1260 and 960 year (750 CE and 1050 CE) have the highest  
 426 overdispersion and are likely less reliable. This could be due to problems specific to the  
 427 dating of young sediments. Because younger sediments are less unconsolidated and less  
 428 dewatered, they are characterized by insufficient luminescence sensitivity to allow  
 429 measurements at very low doses ( $\sim$ tens of mGy) which results in a low signal to noise ratio  
 430 and imprecise doses. Hence, the age of such sediments are often underestimated (Madsen  
 431 and Murray, 2009). This might be the case here as the estimated OSL dates are too young  
 432 compared to our varve chronology ( $368 \text{ CE} \pm 26$  and  $509 \text{ BCE} \pm 28$ ). Therefore, the two  
 433 upper OSL dates have been disregarded. Overall, OSL dating provided only chronological  
 434 control for the basal core sample into the underlying glacial-fluvial deposit but yielded  
 435 overestimates in the overlying sediments.

436  
437

438 **Table 1.** Optically Stimulated Luminescence (OSL) ages\* on quartz from South Sawtooth Lake, Ellesmere Island.

Core/depth	Lab number	Aliquots <sup>a</sup>	Grain-size ( $\mu\text{m}$ )	Equivalent dose (Gray) <sup>b</sup>	Over- dispersion (%) <sup>c</sup>	U (ppm) <sup>d</sup>	Th (ppm) <sup>d</sup>	K (%) <sup>d</sup>	H2O (%)	Cosmic dose rate mGray a <sup>-1</sup>	Dose rate mGray a <sup>-1</sup>	OSL age (a <sup>-1</sup> ) <sup>f</sup>
SSI2-10-1-3P 0-4 cm	BG4055	78/94	20-44	3.21 $\pm$ 0.34	100 $\pm$ 8	3.51 $\pm$ 0.01	13.05 $\pm$ 0.01	2.61 $\pm$ 0.01	35 $\pm$ 5	0.05 $\pm$ 0.005	3.31 $\pm$ 0.17	960 $\pm$ 120
SSI2-10-1-3P 150-154 cm	BG4057	86/99	20-44	3.94 $\pm$ 0.42	116 $\pm$ 20	3.43 $\pm$ 0.01	13.3 $\pm$ 0.01	2.23 $\pm$ 0.01	35 $\pm$ 5	0.03 $\pm$ 0.003	3.03 $\pm$ 0.15	1290 $\pm$ 165
SSI2-10-1-3P 174-178 cm	BG4058	84/112	20-44	8.84 $\pm$ 0.98	72 $\pm$ 20	3.20 $\pm$ 0.01	12.1 $\pm$ 0.01	2.69 $\pm$ 0.01	35 $\pm$ 5	0.03 $\pm$ 0.003	3.25 $\pm$ 0.16	2720 $\pm$ 355
SSI2-12-2-3P 174-178 cm	BG4056	56/68	20-44	27.62 $\pm$ 0.95	22 $\pm$ 2	3.22 $\pm$ 0.01	13.5 $\pm$ 0.01	3.09 $\pm$ 0.01	35 $\pm$ 5	0.03 $\pm$ 0.03	3.62 $\pm$ 0.18	7630 $\pm$ 595

439

440 <sup>a</sup>Aliquots used in equivalent dose calculations versus original aliquots measured.  
 441 <sup>b</sup>Equivalent dose calculated on a pure quartz fraction with about 40-100 grains/aliquot and analyzed under blue-light  
 442 excitation ( $470 \pm 29 \text{ nm}$ ) by single aliquot regeneration protocols (Murray and Wintle, 2003). The central age model of  
 443 Galbraith et al. (1999) was used to calculate equivalent dose when overdispersion values are  $<25\%$  (at one sigma errors;  
 444 a finite mixture model was used with overdispersion with values  $>25\%$  to determine the youngest equivalent dose  
 445 population.  
 446 <sup>c</sup>Values reflect precision beyond instrumental errors; values  $\leq 25\%$  (at 1 sigma limit) indicate low dispersion in equivalent  
 447 dose values and an unimodal distribution.  
 448 <sup>d</sup>OSL dates are referenced to 2010 BCE.  
 449 <sup>e</sup>U, Th and K content analyzed by inductively-coupled plasma-mass spectrometry analyzed by ALS Laboratories, Reno,  
 450 NV; U content includes Rb equivalent.  
 451 <sup>f</sup>Cosmic dose rate calculated from parameters in Prescott and Hutton (1994)

452 <sup>†</sup>Systematic and random errors calculated in a quadrature at one standard deviation. Datum is 2010 CE.

453

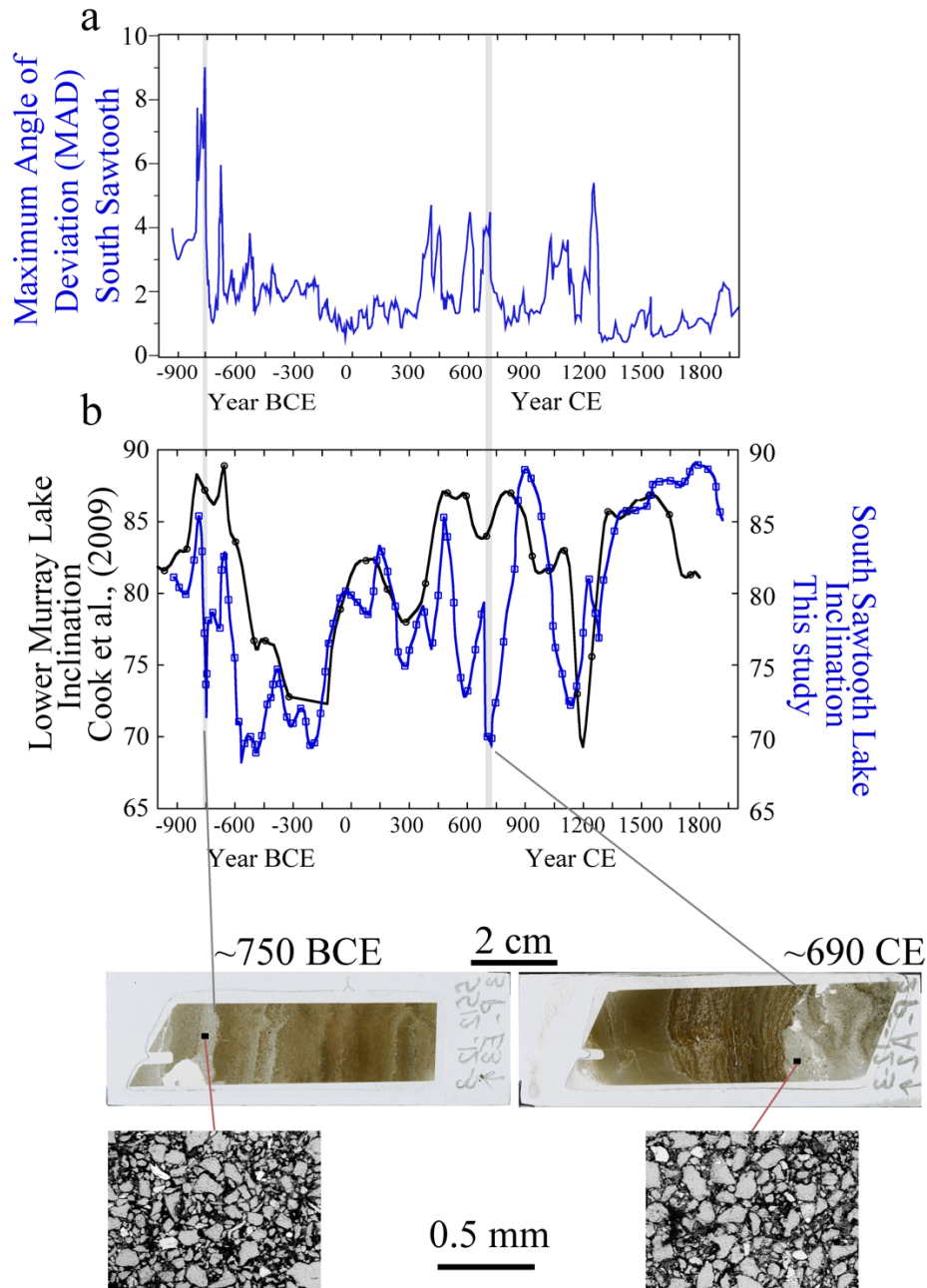
454

### 455 **3.3.3 Paleomagnetic variations**

456

457 Variations of the inclination recorded in the South Sawtooth Lake sediments reveal similar  
458 patterns when compared to Lower Murray Lake (Fig. 7,  $r = 0.45$ ) located 320 km northeast  
459 of SSL (LML: Fig.1a). Intervals where the records are different correspond to thicker than  
460 normal layers (normal being  $<3$  mm which represents 90% of the varve thicknesses) in the  
461 SSL record. Two examples of density flow deposits dated to  $\sim 690$  CE and  $\sim 750$  BCE are  
462 shown in Fig. 7. In these sedimentary facies, fine to medium sand is found at 184.7 and  
463 472.3 cm composite depth, which explains the sharp decrease in inclination values, as  
464 reported by St-Onge et al., (2004) and Valet et al., (2017). When all of the 38 density flow  
465 layers are removed from the analysis, the correlation coefficient slightly increases ( $R=0.48$   
466 without density flows).

467



468

469 Figure 7. Comparison of South Sawtooth and Lower Murray Lakes paleomagnetic  
 470 inclination records. Below : two thin sections (left : SS12-12-3-3P-E3 and right : SS12-12-  
 471 3-2P-A2) showing thick layers with bright coarse sediments (highlighted by two grey bars).  
 472 South Sawtooth Lake inclination data are filtered by a 10-point centered moving average  
 473 to compare to the lower resolution at Lower Murray Lake. Note that the paleomagnetic  
 474 data of SSL are plotted here against this new chronology, while the Lower Murray Lake  
 475 data are plotted according to its original chronology (Cook et al., 2009)

476

477

478

479

480

### 481 **3.3.4 Discussion about the varve chronology**

482

483 Radiometric dating ( $^{210}\text{Pb}$ ) shows excellent agreement with the varve chronology for the  
484 past ~120 years. For longer time scales, as radiocarbon dating is often not reliable in this  
485 type of Arctic environment (Abbott and Stafford, 1996), we looked for alternative dating  
486 methods. Amongst them, samples were extracted for tephrochronology to target the 1362  
487 CE Icelandic volcanic event. Unfortunately, this attempt was not successful. First, SSL is  
488 far from any volcanic source (> 2500 km), unlike the western American coast, where  
489 abundant cryptotephra have been found because of the proximity of volcanic sources (e.g.  
490 Deschamps et al., 2017). Second, SSL sediments are 99% clastic which makes the  
491 extraction of tephra challenging. So far, no lacustrine varve records in the Eastern Canadian  
492 Arctic Archipelago have been validated using tephrochronology to identify a known  
493 volcanic event in the Eastern Canadian Arctic Archipelago. The generally strong co-  
494 variability between the SSL paleomagnetic record and the one from LML (Cook et al.,  
495 2009) supports the SSL varve age model. Indeed, the chronology of LML, through its  
496 paleomagnetic variations, was also confirmed by a well-dated marine sediment archive  
497 from Disraeli Fjord, Ellesmere Island (Antoniades et al., 2011). The age of ~710 BCE  
498 obtained from OSL dating is similar to the paleomagnetic variations of both SSL and LML  
499 providing further support for the chronology in the latter part of our record.

500

501

502

## 503 **3.4 Sediment facies properties**

504

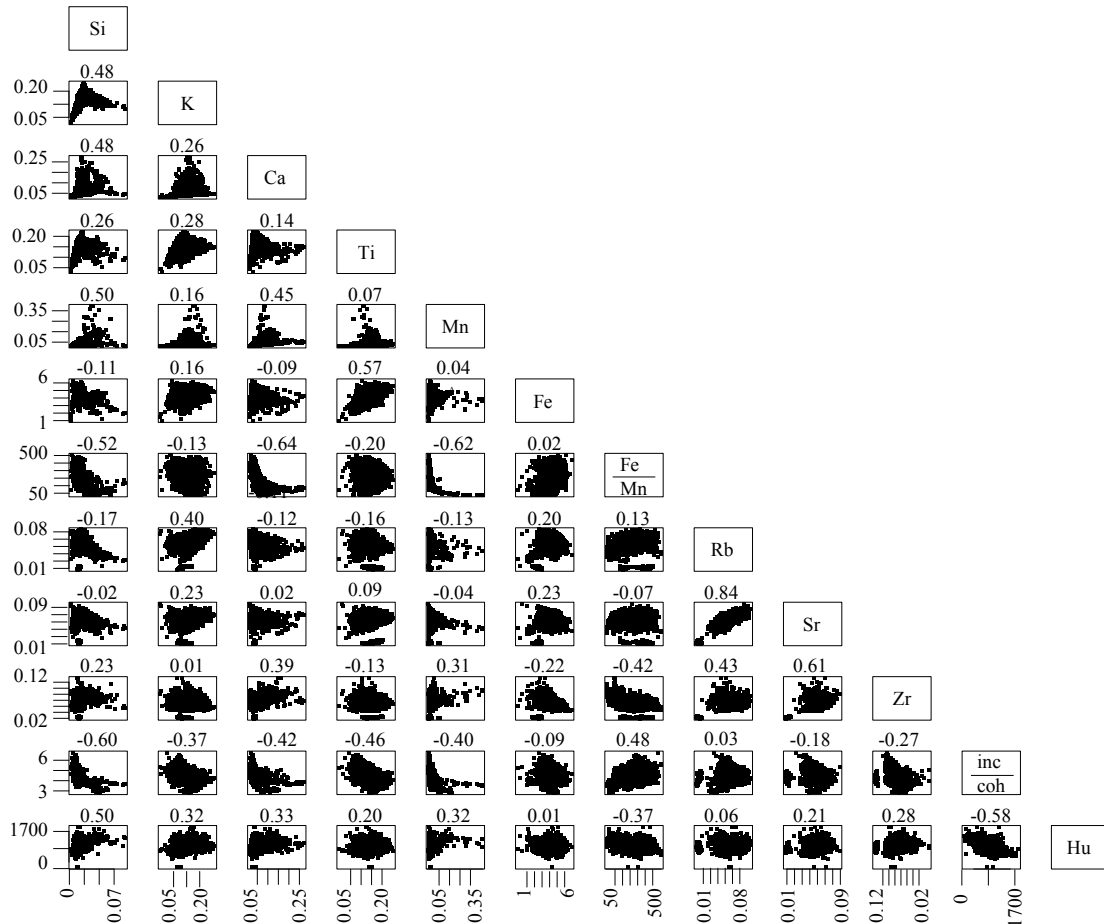
### 505 **3.4.1 $\mu$ -XRF and physical composition of varves**

506

507 Correlation matrix of the elemental composition and the Houndsfield units (HU) is shown  
508 in Figure 8 and Table S4. The inc/coh is defined by the Compton (incoherent) and Rayleigh  
509 (coherent) scattering ratio. Negative correlation between inc/coh and HU indicates that  
510 inc/coh can be used as a density proxy ( $r = -0.58$ ), as was found by Guyard et al., (2007)  
511 and Fortin et al. (2013). Sr and Rb are strongly correlated to each other (Fig. 8 and Table  
512 S4,  $r = 0.84$ ). Sr and Zr are also well correlated ( $r = 0.61$ ) and K is rather poorly correlated  
513 to most of the other elements, except for Rb ( $r = 0.40$ ). As for Fe and Mn, which are often

514 used as a paleo-redox proxy, it can be observed that Fe is highly dependant on detrital input  
 515 since it is correlated to Ti, while Mn is correlated to inc/coh (and HU).

516



517

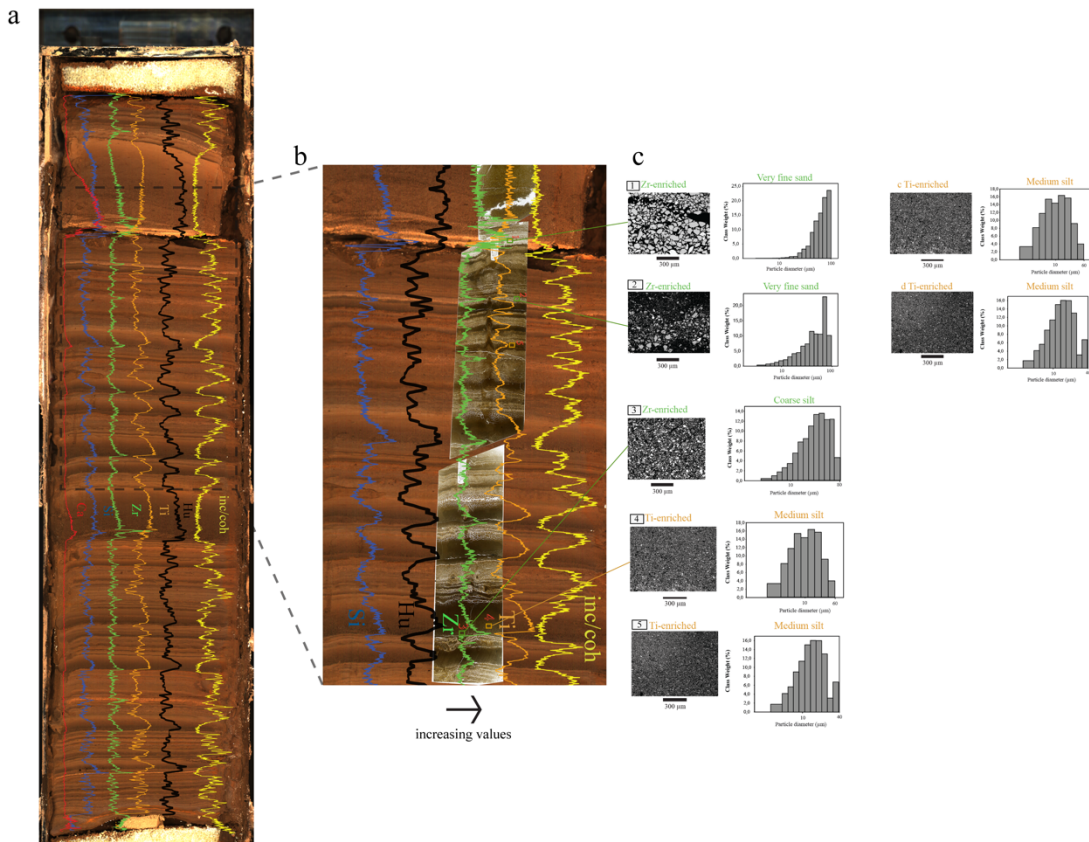
518 Figure 8. A) Scatter plots of the elements at South Sawtooth Lake with CT-Scan  
 519 Houndsfield Units. All resampled data points represent a value integrated over 2 mm (2605  
 520 data points per dataset).

521

522 A similar co-variability is observed between inc/coh, HU, Zr, Ti, Si and Ca, as shown in  
 523 Figure 9. However, Zr increases sharply at the the base of high-energy events as observed  
 524 in the various darker layers (Fig. 9a,b). This pattern is similar to other studies which show  
 525 that Zr is enriched in coarser grain deposits as Zr is associated with heavy and hard minerals  
 526 (Scheffler et al., 2006). This is further confirmed by the backscatter SEM images showing  
 527 Zr enriched in coarse silt to very fine sand layers according to the classification of Folk  
 528 and Ward (1957) (Fig. 9c). The main lithology found where the main inflow is located  
 529 consists of sandstones interstratified with siltstones, and shales with minor amounts of coal.

530 Thus, quartz are a major component of the sediment at Sawtooth Lake. This can be  
 531 observed by the strong co-variability of Si and Zr at the base of many coarse layers (Fig.  
 532 9). Ti is also known to be linked with clastic input, mainly found in fine to medium silty  
 533 layers, as has been reported in many sites (Balascio and Bradley, 2012; Cuven et al., 2010;  
 534 Kylander et al., 2011; McWethy et al., 2010). Both Ti and Zr relate to beds with grain-sizes  
 535 coarser than average, but in graded beds such as turbidites. Ti has lower concentrations at  
 536 the base of turbidites, but increases sharply in thicker layers as the grain-size becomes finer,  
 537 just when Zr starts to decrease upward (Fig. 9). Particle size distribution reveals that Ti is  
 538 enriched in the medium silt layers (Fig. 9c). In general, inc/coh, Ti and HU display similar  
 539 trends and are at higher concentration in high-energy events layer (turbidites), which is  
 540 also the case for Si and Ca. These results are consistent with a previous study on a long  
 541 sediment sequence from Patagonia showing that CT-Scan (HU) and inc/coh provide high-  
 542 resolution and reliable measurements of sediment density variability (Fortin et al., 2013).

543  
 544  
 545



546

547 Figure 9. a) Gravity core SS12-1-1s from SSL showing  $\mu$ -XRF variations of inc/coh  
548 (yellow), Houndsfield Unit (HU; black), Titanium (orange), Zirconium (green), Silicium  
549 (blue) and Calcium (red). b) Blow-up (grey dashed line of a) showing inc/coh, Titanium,  
550 Zirconium, HU and Silicium. The arrow indicates increased values of the parameters  
551 shown. Squares labeled from 1 to 5 are regions of interest photographed at the Scanning  
552 Electron Microscope in backscatter mode (c). c) Backscatter scanning electron microscope  
553 images of the 5 rectangles shown in b with their grain size distribution. Scanning electron  
554 microscope images highlighting coarse silt and fine sand enriched with Zr and medium silt  
555 sediment enriched in Ti.

556

557

558

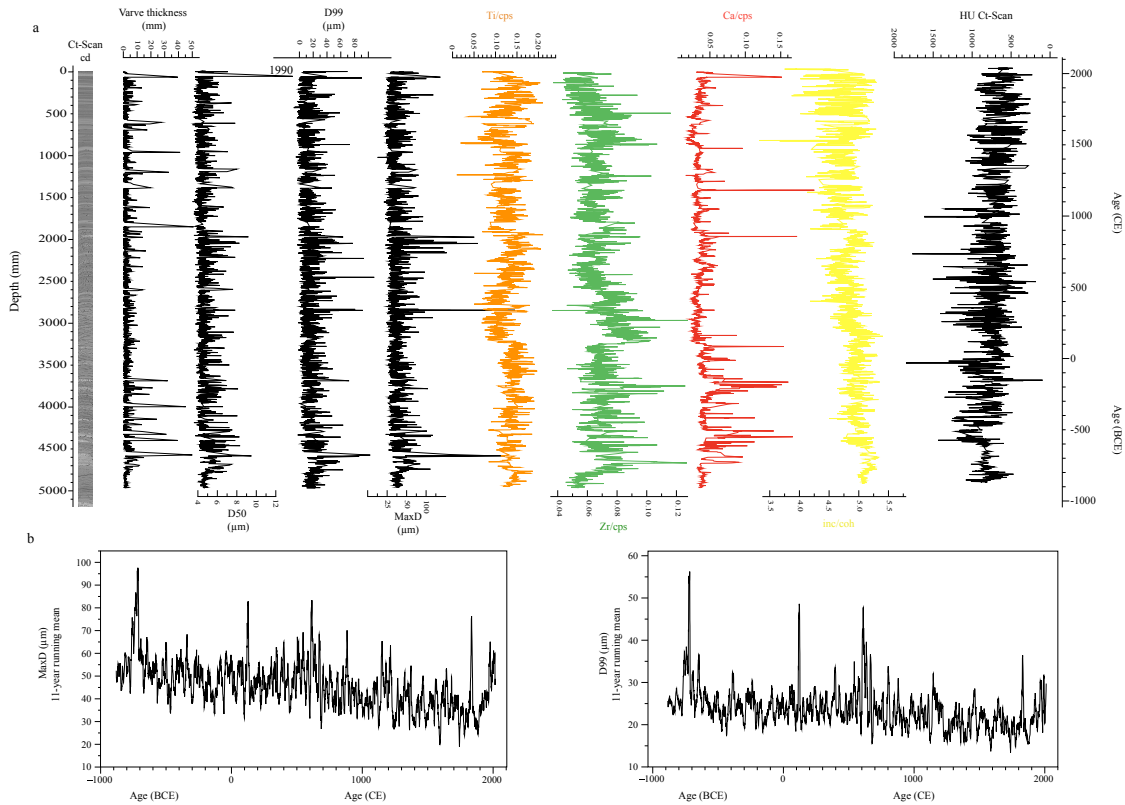
559

### 560 **3.4.2 Stratigraphic trends of sediment properties**

561

562 A general feature in the evolution of the grain-size indices is the overall declining trend in  
563 values from 900 BCE until the beginning of the 20<sup>th</sup> century, when most values increased  
564 with the exception of varve thickness (Figs. 10, S5, Table S5). This is especially evident in  
565 the 50<sup>th</sup> percentile of grain-size showing high values during the 20<sup>th</sup> century and the  
566 coarsest grain-size in 1990 relative to the past 2900 years (Fig. 10a). This general  
567 decreasing trend in grain-size is most visible when a 11 year-running mean is applied to  
568 the series (Fig. 10b). These physical parameters exhibit many common features as shown  
569 in the correlation matrices (Table S3). Some of them show similar characteristics found in  
570 a varve record from Cape Bounty, at East Lake (CBEL) (Lapointe et al., 2012). For  
571 example, the median ( $mD_0$ ) is the grain-size index that exhibits the best correlation with  
572 varve thickness ( $r = 0.42$ ). Similarly, the 99<sup>th</sup> percentile ( $P99D_0$ ) is strongly correlated with  
573 the standard deviation  $sD_0$  ( $r = 0.92$ ) as was observed at Cape Bounty East Lake (Lapointe  
574 et al., 2012).

575



576

577 Figure 10. a) Composite Ct-Scan image of the first ~5 m with grain-size parameters, varve  
 578 thickness, grain-size data (50<sup>th</sup> percentile, 99<sup>th</sup> percentile and the Maximum diameter), μ-  
 579 XRF data and Ct-Scan from South Sawtooth Lake over the past 2900 years. b) MaxD<sub>0</sub> and  
 580 D99 over the past 2900 filtered by an 11 centered running mean.

581

582 The general trend of the annual μ-XRF variations reveals in general a decrease in values  
 583 from 900 BCE to present (Fig. 10a). This is consistent with the particle size data (Figs. 10a,  
 584 S5). For example, Ti and Zr values show a decreasing trend through time, which is also  
 585 reflected in inc/coh (inverted values) and relative density data from the Ct-Scan. We also  
 586 note that the recent (~1850 CE) increase in Zr is not as noticeable as that of the coarse  
 587 grain-size data. While a substantial decreasing trend of Zr around 1500s-present is  
 588 observed, Ca variability shows an increase trend during that time (Fig. 10a). The overall  
 589 correlation between Ca and Zr is significant ( $r = 0.39$ ,  $p < 0.0001$ ). However, when taking  
 590 into account only the past 500 years, a negative correlation is found ( $r = -0.32$ ,  $p < 0.0001$ ).

591

### 592 3.4.3 Discussion about the stratigraphic trends

593

594 The increase in Ca profile on the top of the record appears to point to a different source of  
595 sediment provenance to the lake over the past ~500 years. The lithology in direct contact  
596 with the lake located in the col within the Sawtooth Range consists of sandstones and  
597 calcareous siltstones, with limestones and shales (Geological Survey of Canada, 1972). It  
598 is thus possible that the increase in Ca over the past 500 years is linked with more sediment  
599 deposition from this col area where steep slopes and gullies are present (Fig. 1c). Francus  
600 et al. (2008) hypothesized that sedimentation from that source was expressed as debris  
601 flows triggered by summer rain events. These events produce thin yet coarsened grained  
602 layers. Hence, coarse grain-size and Ca increase during the course of the last 100 years  
603 would mean that summer rain events became more frequent, an interpretation consistent  
604 with a warming climate. The upward decline of the Zr profile suggests that the relative  
605 importance and frequency of snow-melt induced turbidites originating from the main river  
606 watershed that is mainly composed of sandstones and siltstone have declined over the past  
607 100 years. Overall, the results reveal that  $\mu$ -xrf and particle size measurements contain  
608 different information that can inform the interpretation of paleoenvironmental conditions.

609

610 Changes in grain-size mainly reflect changes in snow melt intensity (Francus et al., 2002)  
611 that are influenced by the length of the ice-free season, and therefore summer temperature.  
612 This general decreasing trend in grain-size might thus be attributed to the decrease of  
613 northern hemisphere insolation during the past ~6ka which led to lower hydrological  
614 energy-events available to move sediment in the SSL main river, resulting from lower snow  
615 melt intensity due to decreased temperature (Francus et al., 2002; Kaufman et al., 2004).  
616 The finer fraction ( $< 16 \mu\text{m}$ ) increased from ~1200 CE until 1850 CE (Fig. S5), a period  
617 that corresponds broadly to the Little Ice Age (LIA). The increase in coarse grain-during  
618 the 20<sup>th</sup> century occurs during a similar time interval to the period of pronounced warming  
619 shown in reconstructed Arctic temperature (Kaufman et al., 2009). Indeed, the long-term  
620 declining trend in coarse grain-size has been recently sharply reversed (Fig. 10b). Another  
621 varved sediment record in the Western Canadian Arctic, from Cape Bounty East Lake  
622 (CBEL) also recorded coarse grain-size values during the 20<sup>th</sup> century that reached  
623 unprecedented levels (Lapointe et al., 2012). These changes clearly show that these records  
624 are sensitive indicators of temperature fluctuations. Other periods such as ~800 BCE and

625 ~650 CE in the SSL record also depict strong coarse grain-size anomalies that are higher  
626 than today.

627 Another interesting trend is that varve thickness in the recent part of the record did not  
628 increase at the same pace as the coarse grain-size fraction, another result that is also seen  
629 in the varved record from the western Canadian Arctic (CBEL). Indeed, correlation  
630 between most of the grain-size data and varve thickness is statistically significant but the  
631 strength of the correlation is nevertheless rather weak (Table S3). The reasons that explain  
632 these incompatibilities between the coarse grain-size and varve thickness are not fully  
633 understood. Clearly, thicker varves do not always reflect greater grain-size (Lapointe et al.,  
634 2012, Fig. S6). This might be related to the fact that a varve year can result from multiple  
635 successive snowmelt events with low energy that prevent the transport and deposition of  
636 coarser material (Fig. S6). Conversely, the increase in coarse grain-size and Ca in the past  
637 ~100 years may be linked to more frequent debris flow triggered by summer rainfall that  
638 are not necessarily characterized by thick layers as mentioned above.

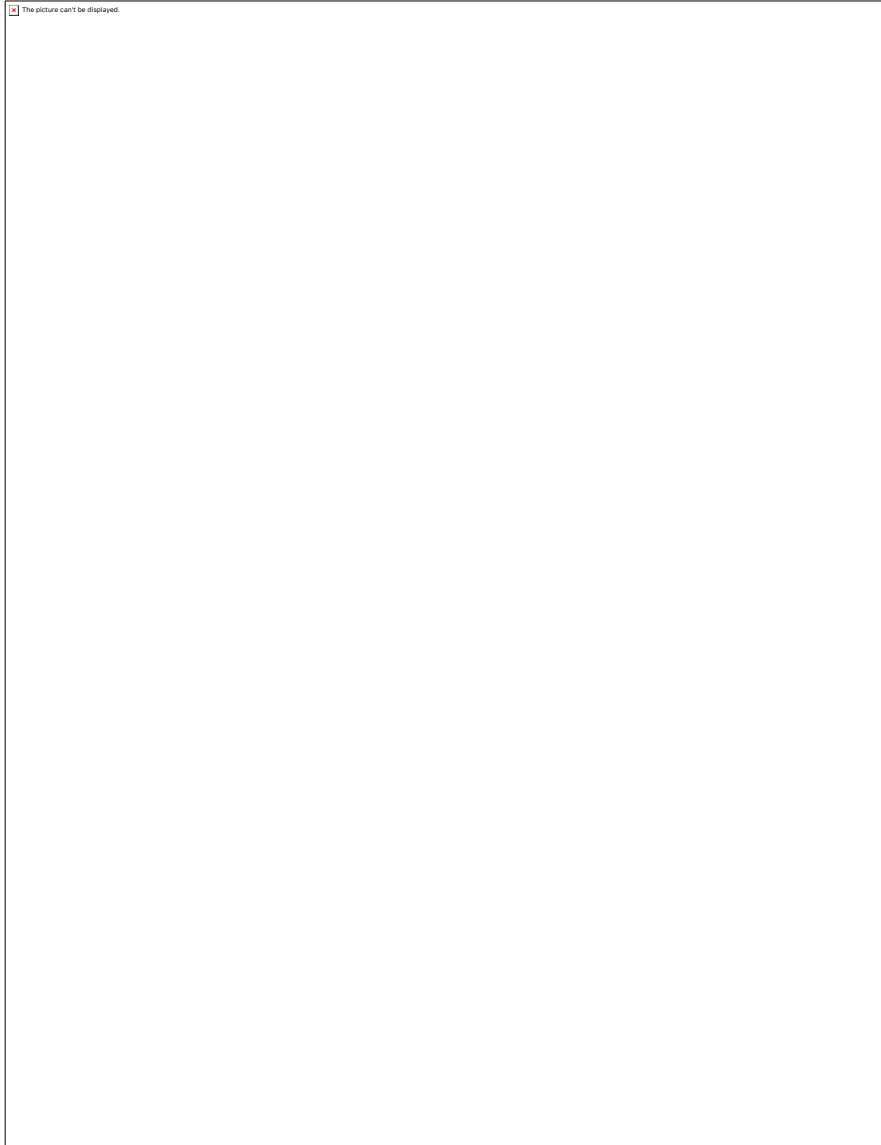
639

640

### 641 **3.5 Comparison of Sawtooth record to meteorological and paleoclimate data**

642

643 PCA analysis indicates that annual sediment elemental variations are different than grain-  
644 size measurements (Fig. 11). The first principal component (related to coarse grain-size)  
645 explains 26% of the variability whereas the second component ( $\mu$ -XRF) accounts for 16%  
646 of the variability. However, some modest but significant correlations between grain-size,  
647 XRF, and Ct-Scan density suggest a common sources of variability among the proxies  
648 (Table 2).



649  
650  
651  
652  
653  
654  
655  
656

Figure 11. Principal components analysis (PCA) of density measurements (inc/coh, HU) and other physical parameters shown in this study. Annual data were normalized relative to the mean and standard deviation.

**Table 2.** Correlation matrix (Pearson) between annual grain-size, Ct-Scan and XRF data over the past 2900 years (A 5-year running average applied to the series to the series to remove noise). Bold values indicate significance <0.05.

657  
658

659 Ti and finer particle size ( $\% < 20 \mu\text{m}$ ) are significantly correlated to PC2 ( $r = 0.87, p <$   
660  $0.0001, r = 0.39, p < 0.01$ ), but moderately anti-correlated to PC1 ( $r = -0.33, p = 0.007, r =$   
661  $-0.79, p < 0.001$ ) over the period of instrumental data (Table S5) (Ti vs PC2 over the past  
662 2900 years :  $r = 0.68, p < 0.0001$ ). The strongest correlation for the PC1 is obtained with  
663 D99 ( $r = 0.96, p < 0.0001$ ) (D99 vs PC1 over the past 2900 years :  $r = 0.90, p < 0.0001$ ).  
664 These results indicate that PC1 reflects coarser grain-size while PC2 is more related to finer  
665 particle size as shown by the significant positive correlation with the fraction  $<20 \mu\text{m}$ , and  
666  $<30 \mu\text{m}$  (Table 3).

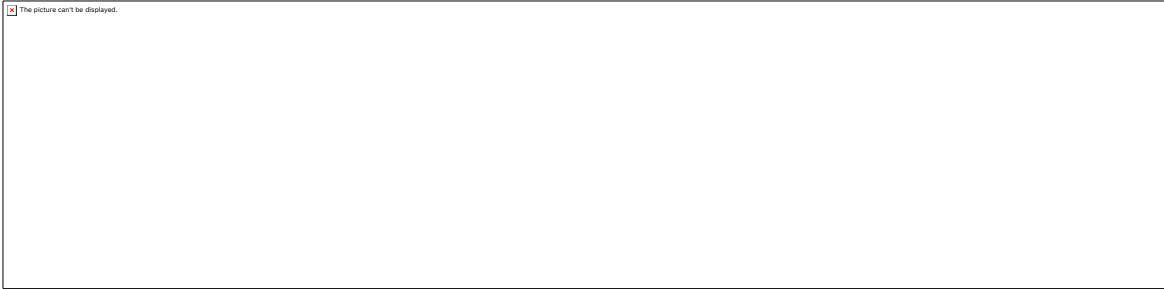
667

668 These data were then compared to the Eureka weather station located at 84 km north-west  
669 of SSL (Fig. 1a). D99 and PC1 (coarse grain-size) are significantly and positively  
670 correlated with May to August temperature from 2011 to 1948 AD (Table 3). An opposite  
671 pattern is observed with PC2 (and Ti) which shows a strong negative link to temperature  
672 ( $r = -0.49, p < 0.001$ ). The variable *snow after 1<sup>st</sup> of June* (SAJ) is defined as the number  
673 of days with snow on the ground following 1<sup>st</sup> of June. It shows a strong negative  
674 correlation with temperature ( $r = -0.60, p < 0.0001$ ), indicating that colder conditions  
675 preserve the snow in the area. The snow melt intensity (SMI) is defined as the maximum  
676 snow depth decrease for a period of 10 days. As shown in Francus et al., (2002), SMI is  
677 more an expression of the rate of change from cold to warm days, and tends to be correlated  
678 to the subsequent duration of summer snow cover (correlation between SMI and SAJ:  $r =$   
679  $0.33, p < 0.001$ ). Thus PC2 is linked to increased SMI characterized by fine to medium  
680 silt deposition in the lake, and thus a proxy for nival melt (Francus et al., 2002), whereas  
681 PC1, characterized by coarser grain-size and debris flow, appears more related to  
682 increasing temperature (Figs. 10cd, 12a).

683

684 **Table 3.** Matrix correlation of selected proxies at SSL including PC1 and PC2 compared to meteorological data from  
685 Eureka weather station 1948-2011 (Bold values are significant at  $p = 0.05$ )

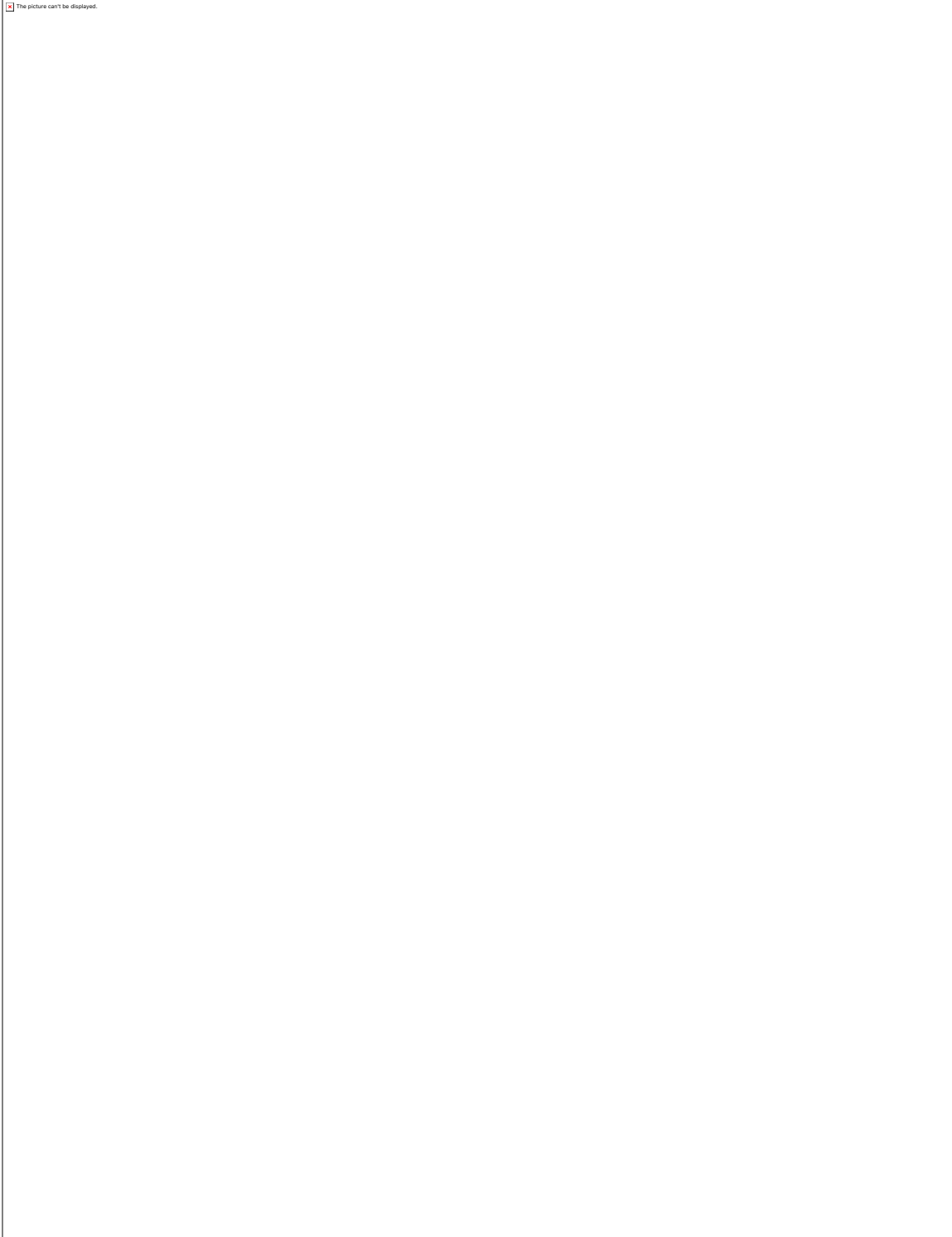
686



687

688 PC1 of the multi-proxies at SSL was compared to the average Agassiz  $\delta^{18}\text{O}$  (Fig. 12b). The  
689  $\delta^{18}\text{O}$  from ice cores is linked to temperature (Jouzel et al., 1997), but also influenced by  
690 changes in moisture source, moisture transport pathways, and precipitation seasonality  
691 (Jouzel et al., 1997, Masson-Delmotte et al., 2005). A significant correlation is observed  
692 during the last 2900 years between PC1 at SSL and  $\delta^{18}\text{O}$  Agassiz record ( $r = 0.65$ ,  $p <$   
693  $0.001$ ). Thus, although PC1 and coarse grain-size are moderately correlated to temperature  
694 during the instrumental record (Table 3), their long-term variability is similar to the  
695 temperature record from Agassiz demonstrating a relatively good proxy for temperature  
696 change on Ellesmere Island.

697 Maximum grain-size diameter ( $\text{maxD}_0$ ) and the 99<sup>th</sup> percentile also show strong co-  
698 variability to the Agassiz  $\delta^{18}\text{O}$  (Figs. 12c, S7). The long-term decline of both records is  
699 consistent with the progressive decrease in northern hemisphere summer insolation at 80°N  
700 (Fig. 12). However, this declining trend increased after ~700 CE and reached minimum  
701 values during the LIA, whereas the older part of the record shows no such trend (Figs. 12,  
702 S7a). This pattern is similar to the overall Arctic Holocene temperature variation from the  
703 22 sites located north of 66°N (Briner et al., 2016). Coldest conditions dominated during  
704 the LIA and appear to have reached lowest values during the early 18<sup>th</sup> century (Fig. 12),  
705 which is also evident from the finer fraction of grain-size (Fig. S5, % < 16  $\mu\text{m}$ ). These  
706 lower grain-size values during the LIA likely reflect less transport energy during that cold  
707 period. By contrast, the sharp increase of coarse grain-size at the turn of the 20<sup>th</sup> century is  
708 coherent with the reconstructed Arctic temperature showing that recent warming has  
709 reversed the long-term cooling trend (Kaufman et al., 2009).



710  
711  
712  
713  
714  
715  
716

Figure 12. a) Comparison between between South Sawtooth Lake PC1 ( $\mu$ -XRF data, Hu, maxDo, D50 and D99) and May to August temperature data from Mould Bay weather station. b) Same as a) but comparing PC1 with Agassiz  $\delta^{18}\text{O}$  (mean of A77-A79-A84-A89 ice cores). c) same as b) but using the maxD<sub>0</sub> grain-size at South Sawtooth Lake. Black and blue curves in c are the 5<sup>th</sup> polynomial degree fit at SSL and Agassiz, respectively.

717 **4 Conclusion**

718

719 This paper presents a new varve chronology from South Sawtooth Lake (SSL), Ellesmere  
720 Island, in the Canadian High Arctic, based on high-resolution varve counting. The varve  
721 chronology is supported by several independent dating methods, namely the  $^{210}\text{Pb}$  and  $^{137}\text{Cs}$   
722 profiles, one OSL date, and paleomagnetic comparison with Lower Murray Lake on  
723 northern Ellesmere Island (Cook et al., 2009). Furthermore, correlations between the SSL  
724 record and the nearby Agassiz Ice Cap  $\delta^{18}\text{O}$  record provides further support that this  
725 chronology is robust and that it can serve as a reference for other archives in the Canadian  
726 High Arctic (for both marine and lake sediments) given its high sedimentation rate of 1.67  
727  $\text{mm a}^{-1}$ . Compared to the other varved records located in the Canadian High Arctic,  
728 sedimentation rates at SSL are the highest reported in this wide region. Although many  
729 paleoclimate reconstructions from varved sediments are still based only on varve thickness,  
730 the results provided here and in a previous study (Lapointe et al., 2012) demonstrate the  
731 value of obtaining annual grain-size data using image analysis. Indeed, the superior  
732 contrast that this approach provides clearly helps to detect thin varves and decreases the  
733 chances of erroneously counting extra-varves (intra-annual layers) thereby increasing the  
734 reliability of varve-based chronologies. Furthermore, obtaining a range of annual grain-  
735 size measurements enables more paleoenvironmental information to be extracted from the  
736 record. Considering that SEM images were crucial in the delineation of thin varves at SSL  
737 to refine the chronology, revisiting other key sites to apply this imaging approach to  
738 sedimentary records could increase the value and fidelity of other long-term varve-based  
739 proxy climate records. Paleomagnetic fluctuations from this site can also be used as a  
740 template for other regional archives where radiocarbon dating has proven to be  
741 problematical. This will benefit the community by increasing the temporal reliability of  
742 regional climate archives for the past  $\sim 3$  millennia. Our record also shows strong  
743 similarities with the nearby  $\delta^{18}\text{O}$  Agassiz Ice Cap, suggesting that the SSL varved record  
744 is sensitive to temperature variability. Finally, this study provides the sedimentological,  
745 stratigraphical and chronological basis for future paleoclimatic reconstructions from SSL  
746 sediments.

747

748

749 **Acknowledgements**

750

751 We wish to thank the Polar Continental Shelf Program for their field logistic support and  
752 NSERC grants to PF and GSO. FL is grateful to grants provided by the W. Garfield Weston  
753 Foundation and the Fond Quebecois de la Recherche sur la Nature et les Technologies. We  
754 also acknowledge support from NSF grant OPP-1744515 to the University of  
755 Massachusetts. Special thanks for Alison MacLeod (University of London) for  
756 cryptotephra analysis. FL would also like to thank Alexandre Normandeau for his help  
757 with the seismic data. We are thankful for the comments of two anonymous reviewers.  
758 Paleo-data used in this study can be found on the NOAA server  
759 <https://www.ncdc.noaa.gov/data-access/paleoclimatology-data/datasets>

760

761

762

763

764

765 **References**

766

767 Abbott, M. B., Stafford T. W., 1996. Radiocarbon geochemistry of modern and ancient  
768 Arctic lake systems, Baffin Island, Canada, *Quat. Res.* 45(3), 300-311.

769

770 Antoniadou, D., Francus P., Pienitz R., St-Onge G., Vincent W. F., 2011. Holocene  
771 dynamics of the Arctic's largest ice shelf, *Proc. Natl. Acad. Sci. Unit. States.*  
772 108(47), 18899-18904.

773

774 Appleby, P., 2002. Chronostratigraphic techniques in recent sediments, in *Tracking  
775 environmental change using lake sediments*, edited, pp. 171-203, Springer.

776

777 Balascio, N. L., and Bradley R. S., 2012. Evaluating Holocene climate change in northern  
778 Norway using sediment records from two contrasting lake systems, *J. paleol.* 48(1),  
779 259-273.

780

781 Bøtter-Jensen, L., E. Bulur, G., Duller., Murray A., 2000. Advances in luminescence  
782 instrument systems, *Radi. Meas.*, 32(5), 523-528.

783

784 Briner, J. P., McKay N. P., Axford Y., Bennike O., Bradley R. S., de Vernal A., Fisher  
785 D., Francus P., Fréchette B., Gajewski K., 2016. Holocene climate change in  
786 Arctic Canada and Greenland, *Quat. Sci. Rev.* 147, 340-364.

787

788 Cohen, J., Screen, J. A., Furtado, J. C., Barlow, M., Whittleston, D., Coumou, D.,  
789 Francis, J., Dethloff, K., Entekhabi, D., Overland J., 2014. Recent Arctic  
790 amplification and extreme mid-latitude weather, *Nat. Geosci.*, 7(9), 627-637.

791

792

793 Cook, T. L., Bradley, R. S., Stoner, J. S., Francus, P., 2009. Five thousand years of  
794 sediment transfer in a high arctic watershed recorded in annually laminated

795 sediments from Lower Murray Lake, Ellesmere Island, Nunavut, Canada, *J. of*  
796 *Paleolim.* 41(1), 77-94.  
797  
798 Croudace, I. Rindby, W., A., Rothwell, R. G., 2006. ITRAX: description and evaluation  
799 of a new multi-function X-ray core scanner, Special Publication-Geological Society  
800 Of London, 267, 51.  
801  
802 Cuvén, S., P. Francus, and S. F. Lamoureux (2010) Estimation of grain size variability  
803 with micro X-ray fluorescence in laminated lacustrine sediments, Cape Bounty,  
804 Canadian High Arctic, *J Paleolimnol*, 44(3), 803-817.  
805  
806 Deschamps, C.-E., St-Onge, G., Montero-Serrano, J.-C., Polyak, L. In press.  
807 Chronostratigraphy and spatial distribution of the Chukchi and Beaufort Seas  
808 magnetic sediments since the last deglaciation. *Boreas*.  
809  
810 Duchesne, M. J., Moore, F., Long, B. F., Labrie, J., 2009. A rapid method for converting  
811 medical Computed Tomography scanner topogram attenuation scale to Hounsfield  
812 Unit scale and to obtain relative density values. *Engi. Geology*, 103(3), 100-105.  
813  
814 Duliu, O. G., 1999. Computer axial tomography in geosciences: an overview. *Earth-Sci.*  
815 *Revi.*, 48(4), 265-281.  
816  
817 Duller, G., 2003. Distinguishing quartz and feldspar in single grain luminescence  
818 measurements. *Radi. Meas*, 37(2), 161-165.  
819  
820 Edlund, S. A., Alt, B.T., 1989. Regional congruence of vegetation and summer climate  
821 patterns in the Queen Elizabeth Islands, Northwest Territories, Canada. *Arctic*, 3-  
822 23.  
823  
824 Fisher, D. A., Koerner R. M., Reeh, N., 1995. Holocene climatic records from Agassiz  
825 ice cap, Ellesmere Island, NWT, Canada. *The Holocene*, 5(1), 19.  
826  
827 Folk, R. L., and Ward W. C., 1957. Brazos River bar: a study in the significance of grain  
828 size parameters. *J Sediment Petrol*, 27 (1), 3-26.  
829  
830 Fortin, D., Francus, P., Gebhardt A. C., Hahn A., Kliem P., Lisé-Pronovost A.,  
831 Roychowdhury R., Labrie, J., St-Onge, G., Team T. P. S., 2013. Destructive and  
832 non-destructive density determination: method comparison and evaluation from the  
833 Laguna Potrok Aike sedimentary record. *Quat. Sci. Revi.* 71, 147-153.  
834  
835 Francus, P., Bradley R. S., Abbott, M. B., Patridge, W., Keimig, F., 2002. Paleoclimate  
836 studies of minerogenic sediments using annually resolved textural parameters.  
837 *Geophys. Res. Lett.* 29 (20), 1998.  
838

839 Francus, P., R. Bradley, T. Lewis, M. Abbott, M. Retelle, and J. Stoner (2008)  
840 Limnological and sedimentary processes at Sawtooth Lake, Canadian High Arctic,  
841 and their influence on varve formation. *J. Paleolim*, 40(3), 963-985.  
842

843 Francus, P., Kanamaru, K. Fortin, D., 2015. Standardization and Calibration of X-  
844 Radiographs Acquired with the ITRAX Core Scanner, in *Micro-XRF Studies of*  
845 *Sediment Cores*, edited, pp. 491-505, Springer.  
846

847 Francus, P., Nobert, P., 2007. An integrated computer system to acquire, process,  
848 measure and store images of laminated sediments., 4th Internat. Limnogeol. Cong.  
849 Barcelona, 11-14th July.  
850

851 Francus, P., Pirard, E., 2004. Testing for sources of errors in quantitative image analysis,  
852 In: Francus P. (ed) *Image analysis, sediments and paleoenvironments*.  
853

854 Galbraith, R. F., Roberts, R. G., Laslett, G. M., Yoshida, H., Olley, J. M., 1999. Optical  
855 dating of single and multiple grains of quartz from Jinmium rock shelter, northern  
856 Australia: Part I, experimental design and statistical models, *Archaeometry*, 41(2),  
857 339-364.

858 Geological Survey of Canada (1972) Geological Map, Canon Fiord, District of Franklin,  
859 Map 1308A, scale 1:250,000.

860 Guyard, H., Chapron, E., St-Onge, G., Anselmetti, F. S., Arnaud, F., Magand, O.,  
861 Francus, P., Mélières, M.A., 2007. High-altitude varve records of abrupt  
862 environmental changes and mining activity over the last 4000 years in the Western  
863 French Alps (Lake Bramant, Grandes Rousses Massif), *Quatern. Sci. Rev.* 26(19),  
864 2644-2660.  
865

866 Husson, F., Josse, J. S. Le, Mazet, J., Husson, M. F., 2016. Package ‘FactoMineR’,  
867 edited, *Obtenido de Multivariate Exploratory Data Analysis and Data Mining:*  
868 <http://cran.r-project.org/web/packages/FactoMineR/FactoMineR>.  
869

870 Jouzel, J., Alley, R. B., Cuffey, K., Dansgaard, W., Grootes, P., Hoffmann, G., Johnsen,  
871 S. J., Koster, R., Peel, D., Shuman, C., 1997. Validity of the temperature  
872 reconstruction from water isotopes in ice cores, *J. Geophys. Res.: Oceans*,  
873 102(C12), 26471-26487.  
874

875 Kaufman, D., Ager, T., Anderson, N., Anderson, P., Andrews, J., Bartlein, P., Brubaker,  
876 L., Coats, L., Cwynar, L. C., Duvall, M., 2004. Holocene thermal maximum in the  
877 western Arctic (0-180°W), *Quat. Sci. Rev.* 23(5-6), 529-560.  
878

879 Kaufman, D. S., Schneider, D. P., McKay, N. P., Ammann, C. M., Bradley, R. S., Briffa,  
880 K. R., Lakes, A., 2009. Recent warming reverses long-term Arctic  
881 cooling. *Science*, 325(5945), 1236-1239.  
882

883 Kylander, M. E., Ampel, L., Wohlfarth, B., Veres, D., 2011. High-resolution X-ray  
884 fluorescence core scanning analysis of Les Echets (France) sedimentary sequence:  
885 new insights from chemical proxies. *J. Quat. Sci.*, 26(1), 109-117.  
886

887 Lapointe, F., Francus, P., Lamoureux, S. F., Saïd, M., Cuvén, S., 2012. 1750 years of  
888 large rainfall events inferred from particle size at East Lake, Cape Bounty, Melville  
889 Island, Canada. *J. Paleolimn.*, 48(1), 159-173.  
890

891 Lapointe, F., Francus, P., Lamoureux, S. F., Vuille, M., Jenny, J. P., Bradley, R. S.,  
892 Massa, C., 2017. Influence of North Pacific decadal variability on the western  
893 Canadian Arctic over the past 700 years. *Clim. Past*, 13(4), 411-420.  
894

895 Lewkowicz, AG., Hartshorn, J., (1998) Terrestrial record of rapid mass movements in the  
896 Sawtooth Range, Ellesmere Island, Northwest Territories, Canada. *Can. J. Earth*  
897 *Sci.* 35.1, 55-64.  
898

899 Lewis, T., Braun, C., Hardy, D. R., Francus, P., Bradley, R. S. 2005. An extreme  
900 sediment transfer event in a Canadian High Arctic stream. *Arc. Antarc. Alp. Res.*  
901 37(4), 477-482.  
902

903 Madsen, A. T., Murray, A. S. 2009. Optically stimulated luminescence dating of young  
904 sediments: a review, *Geomorph.* 109(1), 3-16.  
905

906 Major, J.J. 2003. Debris flow. In: Middleton GV (ed) *Encyclopedia of sediments and*  
907 *sedimentary rocks.* Kluwer, Dordrecht, pp 186–188

908

909 Masson-Delmotte, V., Landais, A., Stievenard, M., Cattani, O., Falourd, S., Jouzel, J.,  
910 Johnsen, S. J, Dahl-Jensen, D., Sveinbjornsdottir, A., White, J., 2005. Holocene  
911 climatic changes in Greenland: Different deuterium excess signals at Greenland  
912 Ice Core Project (GRIP) and North GRIP, *J. Geophys. Res.: Atmos.* 110(D14).  
913

914 McWethy, D. B., Whitlock, C., Wilmshurst, J. M., McGlone, M. S., Fromont, M., Li, X.,  
915 Dieffenbacher-Krall, A., Hobbs, W. O., Fritz, S. C., Cook, E. R., 2010. Rapid  
916 landscape transformation in South Island, New Zealand, following initial  
917 Polynesian settlement, *Proc. Nati. Acad. Sci. Unit. States.* 107(50), 21343-21348.  
918

919 Mejdahl, V., Christiansen, H. H., 1994. Procedures used for luminescence dating of  
920 sediments, *Quat. Sci. Revi.* 13(5-7), 403-406.  
921

922 Mulder, T., Alexander, J., 2001. The physical character of subaqueous sedimentary  
923 density flows and their deposits. *Sedimentology* 48.2: 269-299.  
924

- 925 Murray, A. S., Olley, J. M., 2002. Precision and accuracy in the optically stimulated  
926 luminescence dating of sedimentary quartz: a status review. *Geochronometria*,  
927 21(1), 1-16.  
928
- 929 Murray, A. S., Wintle, A. G., 2003. The single aliquot regenerative dose protocol:  
930 potential for improvements in reliability. *Radi. Meas.* 37(4), 377-381.  
931
- 932 Normandeau, A., Brown, O., Jarrett, K., Francus, P., De Coninck, A., 2019. Epoxy  
933 impregnation of unconsolidated marine sediment core subsamples for the  
934 preparation of thin sections at the Geological Survey of Canada (Atlantic),  
935 Geological Survey of Canada, Technical Note 10, 10 p.  
936 <https://doi.org/10.4095/313055>  
937
- 938 Ojala, A., Francus, P., Zolitschka, B., Besonen, M., Lamoureux, S. 2012. Characteristics  
939 of sedimentary varve chronologies—a review. *Quat. Sci. Revi.* 43, 45-60.  
940
- 941 Olley, J. M., De Deckker, P., Roberts, R. G., Fifield, L. K., Yoshida, H., Hancock, G.,  
942 2004. Optical dating of deep-sea sediments using single grains of quartz: a  
943 comparison with radiocarbon. *Sedi. Geol.* 169(3), 175-189.  
944
- 945 PAGES 2k 2013. Continental-scale temperature variability during the past two millennia,  
946 *Nature Geosci.*  
947
- 948 Perren, B. B., Bradley, R. S., Francus, P., 2003. Rapid lacustrine response to recent High  
949 Arctic warming: a diatom record from Sawtooth Lake, Ellesmere Island, Nunavut.  
950 *Arc. Antarc. Alp. Res.* 35(3), 271-278.  
951
- 952 Prescott, J. R., Hutton, J. T., 1994. Cosmic ray contributions to dose rates for  
953 luminescence and ESR dating: large depths and long-term time variations. *Radi.*  
954 *Meas.* 23(2-3), 497-500.  
955
- 956 Scheffler, K., D. Buehmann, Schwark, L. 2006. Analysis of late Palaeozoic glacial to  
957 postglacial sedimentary successions in South Africa by geochemical proxies—  
958 response to climate evolution and sedimentary environment. *Palaeogeo.*  
959 *Palaeoclim. Palaeoec.* 240(1), 184-203.  
960
- 961 Smith, S.V., Bradley, R.S., Abbott, M.B., 2004. A 300 year record of environmental  
962 change from Lake Tuborg, Ellesmere Island, Nunavut, Canada. *J.*  
963 *Paleolimn.* 32(2), pp.137-148.  
964
- 965 St-Onge, G., Mulder, T. Piper, D. J., Hillaire-Marcel, C., Stoner, J. S., 2004. Earthquake  
966 and flood-induced turbidites in the Saguenay Fjord (Québec): a Holocene  
967 paleoseismicity record. *Quat. Sci. Revi.* 23(3), 283-294.  
968
- 969 Valet, J.-P., Tanty, C., Carlut, J., 2017. Detrital magnetization of laboratory-redeposited  
970 sediments, *Geophys. J. Intern.* 210(1), 34-41.

971  
972 Vinther, B. M., Buchardt, S. L., Clausen, H. B., Dahl-Jensen, D., Johnsen, S. J., Fisher,  
973 D., Koerner, R., Raynaud, D., Lipenkov, V., Andersen, K., 2009. Holocene  
974 thinning of the Greenland ice sheet. *Nature*, 461(7262), 385-388.  
975  
976 Vinther, B. M., Clausen, H. B., Fisher, D. A., Koerner, R. M., Johnsen, S. J., Andersen,  
977 K. K., Dahl-Jensen, D., Rasmussen, S. O., Steffensen, J. P., Svensson, A. M., 2008.  
978 Synchronizing ice cores from the Renland and Agassiz ice caps to the Greenland  
979 Ice Core Chronology, *J. Geophys. Res. D: Atmos.*, 113(8).  
980  
981 Wright, D. K., Forman, S. L., Waters, M. R., Ravesloot, J. C., 2011. Holocene eolian  
982 activation as a proxy for broad-scale landscape change on the Gila River Indian  
983 Community, Arizona. *Quat. Res.*, 76(1), 10-21.  
984  
985 Xuan, C., and J. E. Channell (2009) UPmag: MATLAB software for viewing and  
986 processing u channel or other pass-through paleomagnetic data, *Geochem. Geophys.*  
987 *Geosyst.* 10(10).  
988  
989 Zolitschka, B., Francus, P., Ojala, A. E., Schimmelmann, A. 2015. Varves in lake  
990 sediments—a review. *Quat. Sci. Revi.*, 117, 1-41.  
991  
992  
993  
994  
995  
996  
997  
998  
999  
1000  
1001  
1002  
1003  
1004  
1005  
1006  
1007  
1008  
1009  
1010  
1011  
1012  
1013  
1014  
1015

1016

1017 **Supplementary information**

1018

1019 **Optically Stimulated Luminescence (OSL)**

1020

1021 A series of experiments was performed to evaluate the effect of preheating at 180, 200,  
1022 220, 240 and 260 °C on isolating the most robust time-sensitive emissions and thermal  
1023 transfer of the regenerative signal prior to the application of SAR dating protocols (see  
1024 Murray and Wintle, 2003). These experiments entailed giving a known dose (25 Gy) and  
1025 evaluating which preheat resulted in recovery of this dose. There was concordance with  
1026 the known dose (25 Gy) for preheat temperatures above 200 °C with an initial preheat  
1027 temperature used of 220 °C for 10 s in the SAR protocols. A “cut heat” at 160 °C for 10 s  
1028 was applied prior to the measurement of the test dose and a final heating at 260 °C for 40  
1029 s was applied to minimize carryover of luminescence to the succession of regenerative  
1030 doses. A test for dose reproducibility was also performed following procedures of Murray  
1031 and Wintle (2003) with the initial and final regenerative dose of 6.6 Gy yielding concordant  
1032 luminescence responses (at one-sigma error). Calculation of equivalent dose by the single  
1033 aliquot protocols was accomplished for 25 to 37 aliquots. For all samples 75 to 85%  
1034 aliquots were used to define the final ( $D_e$ ) distribution and age determination; aliquots were  
1035 removed from analysis when the recycling ratio was not between 0.90 and 1.10, the zero  
1036 dose was > 5% of the natural emissions or the error in equivalent dose determination is  
1037 >10%. Equivalent dose ( $D_e$ ) distributions were log normal and exhibited a range of  
1038 overdispersion values from 116 to 22% (Table 1). An overdispersion percentage of a  $D_e$   
1039 distribution is an estimate of the relative standard deviation from a central  $D_e$  value in  
1040 context of a statistical estimate of errors (Galbraith et al., 1999; Galbraith and Roberts,  
1041 2012). A zero overdispersion percentage indicates high internal consistency in  $D_e$  values  
1042 with 95% of the  $D_e$  values within  $2\sigma$  errors. Overdispersion values  $\leq 25\%$  are routinely  
1043 assessed for small aliquots of quartz grains that are well solar reset, like eolian sands (e.g.,  
1044 Olley et al., 2004; Wright et al., 2011; Meier et al., 2013) and this value is considered a  
1045 threshold metric for calculation of a  $D_e$  value using the central age model of Galbraith et  
1046 al. (1999). Overdispersion values >20% (at two sigma limits) indicate mixing or grains of  
1047 various ages or partial solar resetting of grains; a finite mixture model is an appropriate  
1048 statistical treatment for such data (Galbraith and Green, 1990). All SAR emissions were

1049 integrated over the first 0.8s of stimulation out of 40 seconds of measurement, with  
1050 background based on emissions for the last 30- to 40-second interval. The luminescence  
1051 emission for all quartz sands showed a dominance of a fast component (see Murray and  
1052 Wintle, 2003) with > 90% diminution of luminescence after 4 seconds of excitation with  
1053 blue light.

1054

1055 A determination of the environmental dose rate is needed to render an optical age, which  
1056 is an estimate of the exposure of quartz grains to ionizing radiation from U and Th decay  
1057 series, <sup>40</sup>K, and cosmic sources during the burial period (Table 1).

1058

1059

1060

1061

1062

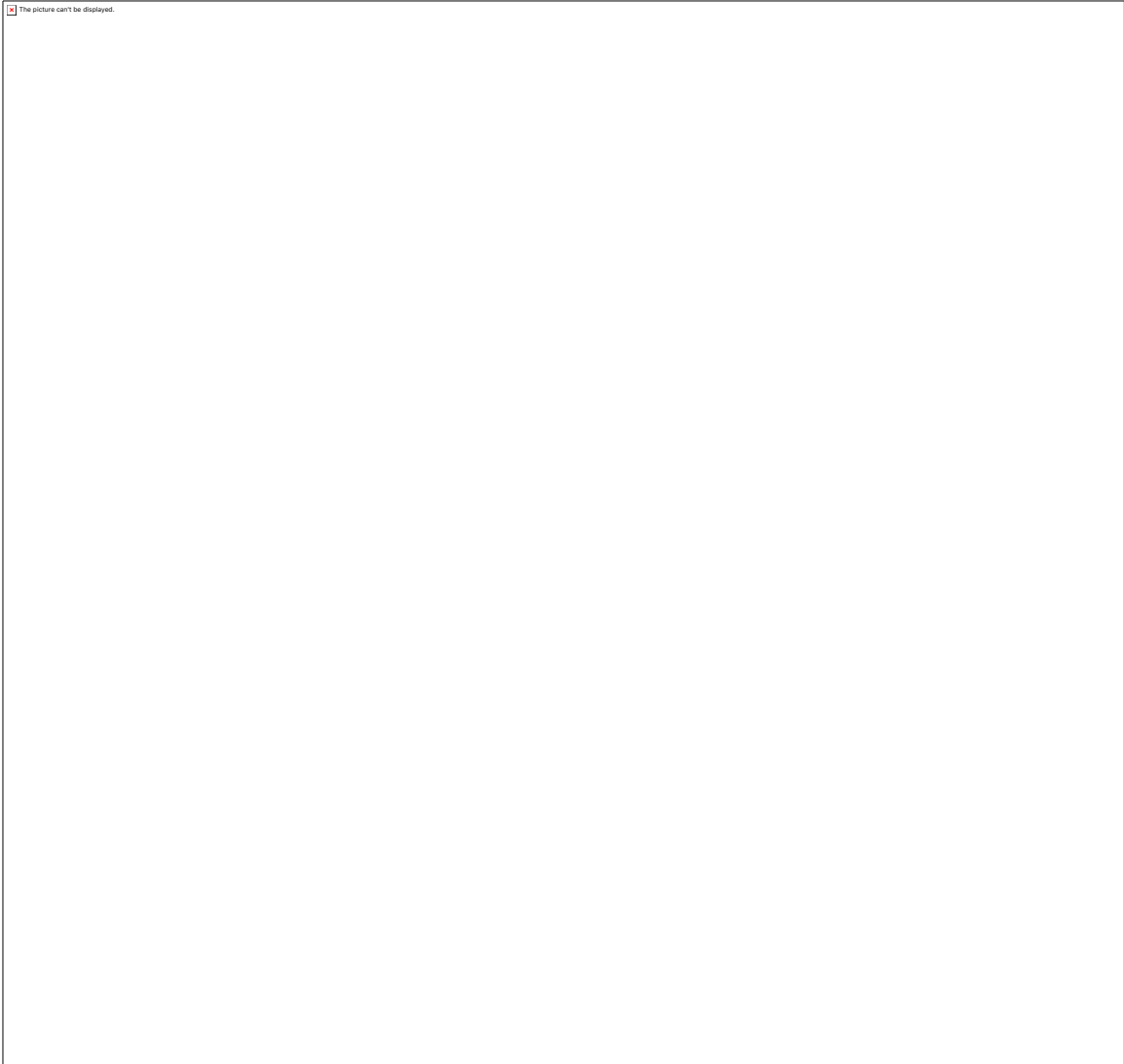
1063

1064

1065

1066

1067



1068

1069 Figure S1. Sediment cores from South Sawtooth Lake with corresponding thin-sections  
1070 used in this study to be a composite profile.

1071



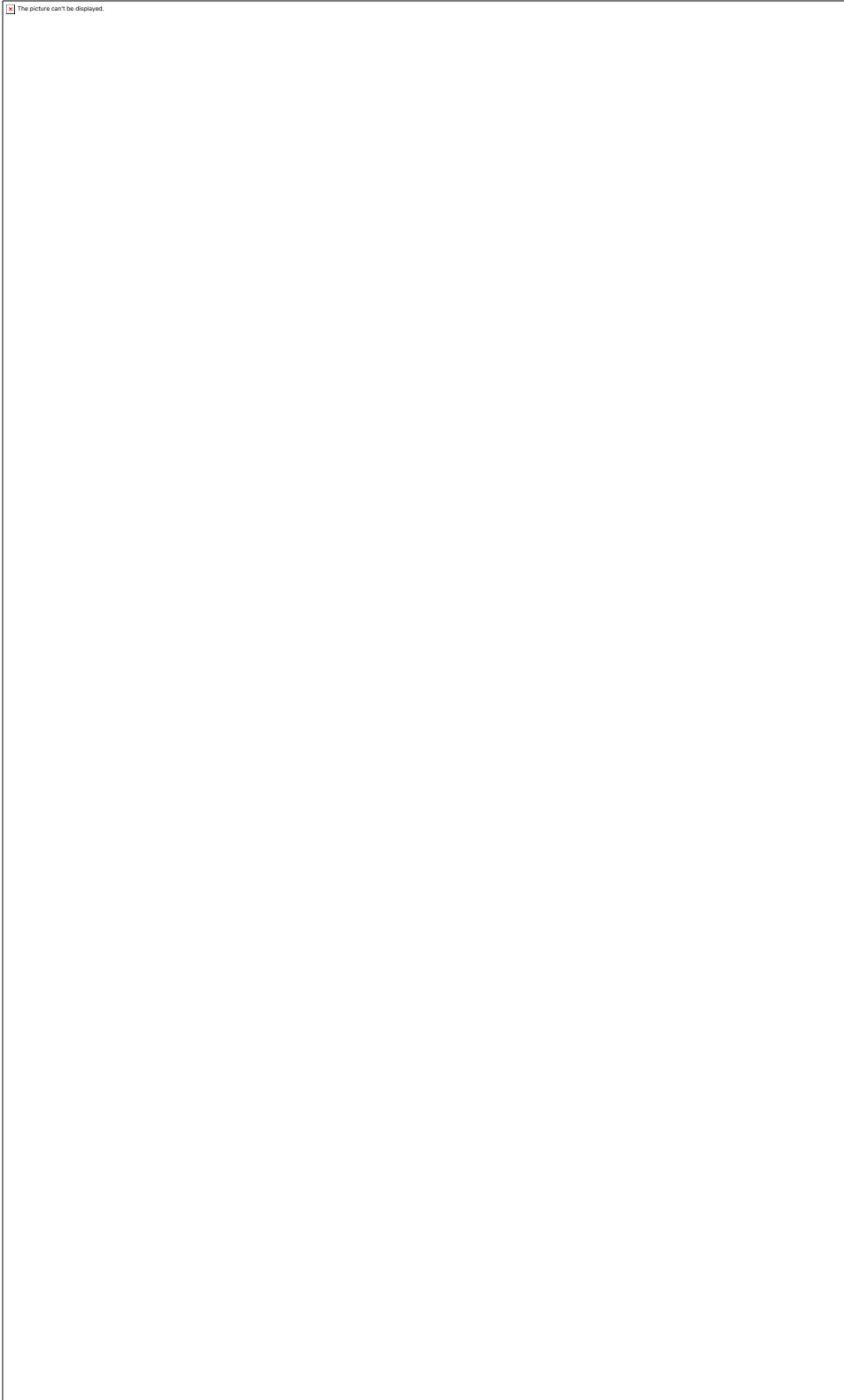
1072

1073 Figure S2. A: thin section SS12-12-2-2P-D1. Red square delimits seven ROIs. At right:  
1074 SEM-images of the corresponding ROIs with the median grain-size. SEM-images clearly  
1075 helps to identify clay caps associated with winter. In this case 2 clay caps are observed  
1076 (shaded grey rectangles).  
1077



1078  
1079  
1080

Figure S3. Intervals where varved are difficult to delineate (diffuse varves) with optical images of thin sections only. Highlighted by black rectangles



1081  
1082  
1083  
1084

Figure S4. Intervals with successive layers considered as being one single varve highlighted by the black rectangles.

1085

1086 Table S1. Statistical descriptors of the varve thickness series

Variable	Minimum	Maximum	Average	Standard deviation
VT	0.106	50.900	1.672	2.981

1087

1088

1089

1090

1091 Table S2. Statistical analysis of the distribution frequency of the varve thickness series.

Percentile	Value
<b>Maximum</b>	
100%	50,900
99%	13,410
95%	4,995
90%	3,158
<b>3rd Quartile</b>	
75%	1,672
<b>Median 50%</b>	
	0,963
<b>1st Quartile</b>	
25%	0,593
10%	0,381
5%	0,296
1%	0,191
<b>Minimum 0%</b>	
	0,106

1092

1093

1094

1095

1096 **Table S3.** Pearson’s correlation between varve thickness and the grain-size indexes over  
1097 the past 2900 years. Bold values indicate significant correlation ( $p < 0.05$ )

1098



1099

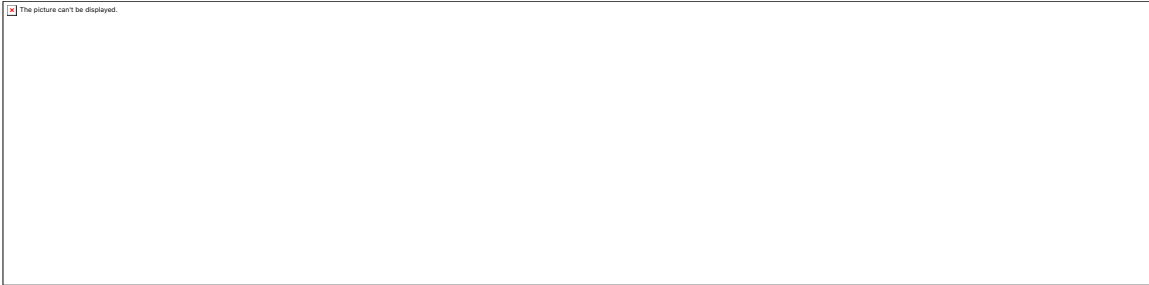
1100

1101

1102

1103  
1104  
1105  
1106  
1107  
1108  
1109  
1110  
1111

**Table S4.** Correlation matrix between  $\mu$ -xrf and Ct-Scan data. Bold values indicate significant correlation ( $<0.0001$ ). Note that all data are resampled at 2mm scale to allow comparison and each dataset has 2605 data points covering the upper 521 cm of the composite section.



1112  
  
1113  
1114  
1115  
1116  
1117  
1118  
1119  
1120  
1121  
1122  
1123  
1124  
1125  
1126  
1127  
1128  
1129  
1130  
1131  
1132  
1133  
1134  
1135  
1136  
1137  
1138  
1139

1140  
1141  
1142  
1143  
1144  
1145  
1146  
1147



1148  
1149  
1150  
1151  
1152  
1153  
1154  
1155  
1156  
1157  
1158  
1159

Figure S5. 2900 years of varve thickness (VT) and annual grain-size variations. Data are filtered by a 5-year running-mean.

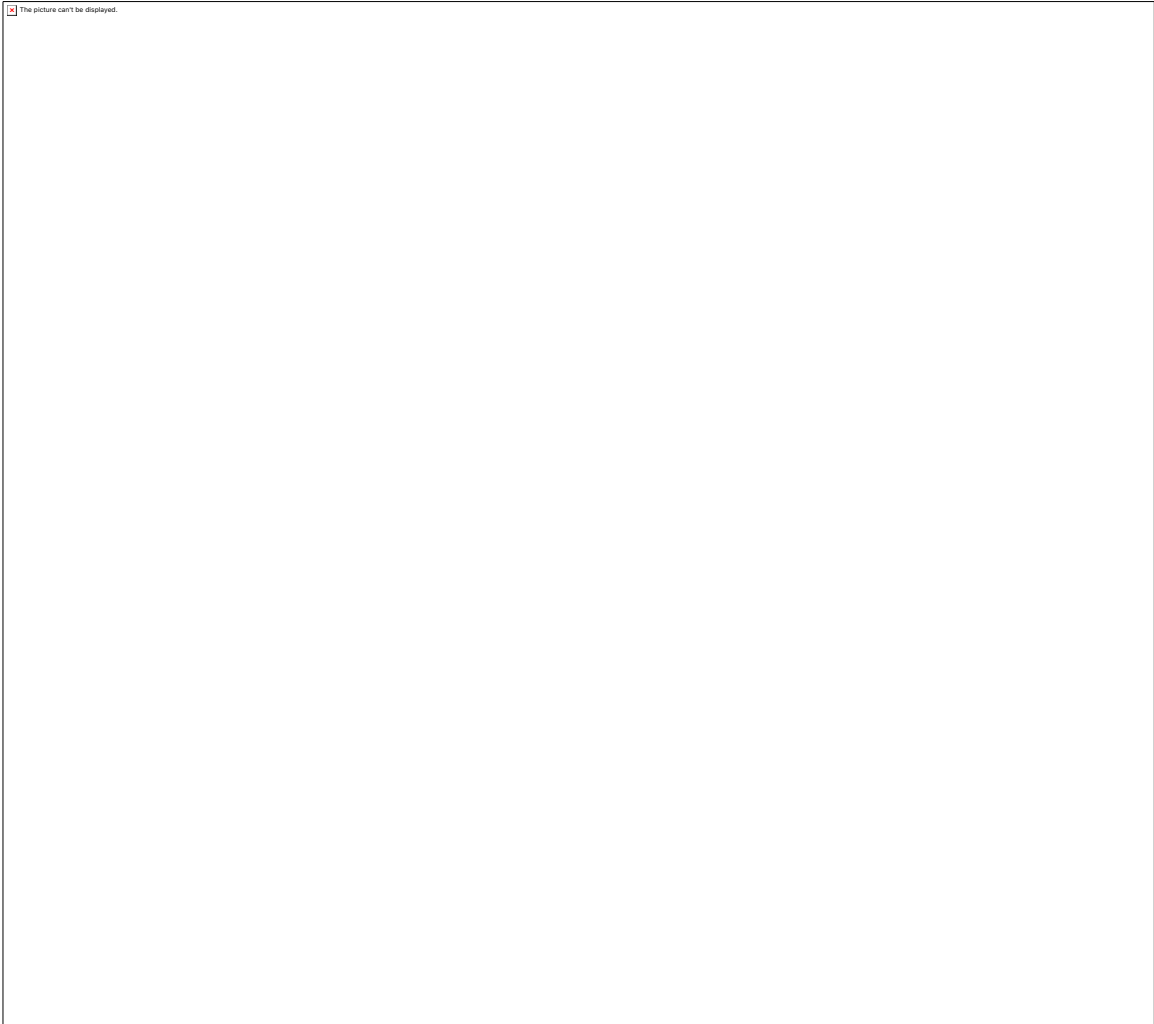
1160  
1161

Table S5. Linear regression slope for varve thickness (VT) and some grain-size fractions for the period 900 BCE – 1900 CE.



1162

1163  
1164



1165  
1166  
1167  
1168  
1169  
1170  
1171  
1172

Figure S6. Overlapping thin section ss12-12-2-1s-D1 and D2. At right: SEM-images of the corresponding black rectangle. 1) is a thick varve with successive layers but finer sediment than in 4) which shows a thin varve but coarser sediment.



1173  
1174  
1175  
1176  
1177  
1178

Figure S7. Upper panel: Comparison between South Sawtooth Lake (99th percentile) and Agassiz  $\delta^{18}\text{O}$  (A77). (b), same as (a) but data are detrended. Data from South Sawtooth Lake are averaged every 25 years to allow comparison.